University of Crete

Department of Materials
Science and Technology

Diploma Thesis for the
Degree of Master of Science

High Resolution Optical Topography

Matina Vlachou

Supervisor: Professor Dimitris Papazoglou

October 2019

Acknowledgements

First and foremost, I would like to express my sincere gratitude to my supervisor Professor Dimitris Papazoglou, for his continuous support, in all aspects of this project, the past two years. His inspiration, guidance and encouragement have been invaluable in completing this work.

I would like to thank Professor Dimitris Anglos and Professor George Kioseoglou, members of my thesis committee, for their interest in my work.

I wish to acknowledge financial support from the Heracles project, and thank principal investigator Dr. Vivi Pouli. I would like to thank Alina Melissanaki and Kostas Hatzigiannakis, members of the project, for their support.

Furthermore, I would like to thank Vangelis Tzardis, fellow graduate student in our group, whose contribution in this work was important, since he developed a robust algorithm for data analysis.

I wish to thank Dimitris Mansur, PhD candidate and member of our group, for his always willing help and appreciated support.

For their help in providing me with samples, I would like to thank Researcher Maria Farsari, Dr. Areti Mourka, Vangelis Skoulas, Antonis Papadopoulos, and Dimitris Theodoridis.

I also wish to thank the members of our group, Michalis Loulakis, Tasos Kouloukidis, Christina Daskalaki and Mikis Milonakis, for their help and useful discussions.

Last but not least, I would like to thank my friends Matina and Manolis for their moral support, my companion Giorgos Miltos for his continuous encouragement and invaluable help, and of course my family for their ever-present and precious love and support.

Abstract

Surface topography is an important aspect of materials science and engineering research with applications ranging from coatings, tribology, engineered or structured surfaces, to traceology of archaeological surfaces. Using portable, non-invasive high resolution techniques, which enable in-line measurements, is advantageous in many of these applications. Furthermore, the ability to perform rapid, high repetition rate measurements is a prerequisite for studying the temporal evolution of minute topographic changes.

For this purpose a portable optical profilometer based on interferometry was designed and developed. By studying the spectral modulation, which results from the interference of white light reflected from the sample's surface and a reference surface, we are able to retrieve the surface profile along a line without using any moving parts. As we demonstrate our profilometer can perform measurements, at a rate that exceeds 170 fps, with a resolution better that 10 nm in the longitudinal direction (80 dB dynamic measurement range) and 8 μm in the transverse over a field of 3 mm. By measuring a variety of surfaces we show that spectral interferometry is a powerful, nondestructive technique ideal for performing rapid, high-resolution measurements of both smooth and abrupt surface variations with no restrictions in the surface hardness.

Contents

List of Abbreviations

CCD	Charge Coupled Device
OPD	Optical Path Difference
LED	Light Emitting Diode
L	Lens
M	Mirror
S	Source
WLI	White Light Intrferometry
BS	Beam Splitter
STM	Scanning Tunneling Micropy
SPM	Scanning Probe Microscopy
AFM	Atomic Force Microscopy
NSOM	Near-field Scanning Optical Microscopy
SEM	Scanning Electron Microscopy
TEM	Transmission Electron Microscope

Chapter 1

Introduction to Wave Optics

1.1 Electromagnetic Radiation

Electromagnetic radiation refers to the waves or the quanta (photons) of the electromagnetic field, propagating through space and carrying energy. Like all elementary particles, photons are currently best explained by quantum mechanics, exhibiting wave-particle duality, i.e. properties of both waves and particles. Both attributes may not be revealed in a single measurement. Certain phenomena, such as interference, exhibit the wave character of light, whereas other, such as the photoelectric effect, display the particle aspect. Broadly speaking, light propagation in free space and other media can be described in classical terms by Maxwell's Electromagnetic Theory, whereas light-matter interaction (absorption and emission of light) can be understood by Quantum Theory. The combined theory is known as Quantum Electrodynamics (QED) (Fowles 1989, p. 2-3, Sharma 2006, p. 1).

Particle-like Behavior

Photons have zero rest mass and move at the speed of light, $c = 2.9979 \cdot 10^8 m/s$, within vacuum. They transport energy and momentum equal to

$$E = hf = \frac{hc}{\lambda} \quad (c = \lambda f), \quad p = \frac{E}{c}, \tag{1.1}$$

respectively, where h is Planck's constant and f is the radiation frequency.

Wave-like Behavior

An electromagnetic wave consists of coupled oscillating electric and magnetic fields, with the following properties (Purcell & Morin 2013, p. 440-441):

(1) The field pattern travels with the speed of light,

(2) At every point in the wave at any instant of time, the electric field strength equals c times the magnetic field strength,

$$E = c \cdot B \tag{1.2}$$

(3) The electric field and the magnetic field are perpendicular to one another and to the direction of propagation. In other words, a wave travels in the direction of the vector $\vec{E} \times \vec{B}$.

Light

Light usually refers to the electromagnetic radiation within the visible spectrum (between the infrared and the ultraviolet), responsible for the sense of human sight. The visible portion of the electromagnetic spectrum is usually approximately defined in the range $380 - 740$ nm, $405 - 790$ THz, and $1.65 - 3.1$ eV, for the photon wavelength, frequency, and energy, respectively.

1.2 Monochromatic Light

Let us consider light vibrations in an optical field. We may represent them by a scalar U(t), at a point in the field (Wolf 2007, p. 1). If the light was monochromatic, it would be expressed as

$$U(t) = \alpha \cdot cos(\phi - \omega t), \tag{1.3}$$

where α is constant and denotes the amplitude, ϕ is the phase, ω is the frequency, and t denotes time.

However, monochromatic sources and fields are an idealization which is never encountered in nature or in a laboratory. Practical light sources have spectral bandwidths varying from a fraction of a kHz for a good single mode laser, to the broad spectrum of a black body radiator.

Light that in some respects imitates monochromatic light most closely is so-called quasi-monochromatic light. It is defined by the property that its effective bandwidth $\Delta\omega$ is much smaller than its mean frequency $\bar{\omega}$, i.e.

$$\Delta\omega << \bar{\omega}. \tag{1.4}$$

.

For such light, the amplitude and phase can no longer be considered constant, and its vibrations at a point in space may be represented by a generalization of Eq. 1.3, viz.,

$$U(t) = \alpha(t) \cdot cos[\phi(t) - \bar{\omega}t] \tag{1.5}$$

where the amplitude $\alpha(t)$ and the phase $\phi(t)$ now depend on time and may fluctuate. We assume we are dealing with a 'steady-state' field: a statistically stationary field for which the statistical behavior that underlies its fluctuations does not change over the course of time.

1.3 Interference of Light Waves

When two or more light waves overlap, the resultant field, given by the superposition principle, is the vector sum of the fields associated with the individual waves, i.e.

$$\vec{E}(\vec{r},t) = \sum_i \vec{E}_i(\vec{r},t), \tag{1.6}$$

where $\vec{E}_i(\vec{r},t)$ is the electric field associated with the ith wave.

Optical interference corresponds to the interaction of two or more lightwaves yielding a resultant irradiance that deviates from the sum of the component irradiances (Hecht 2017, p. 390, Sharma 2006, p. 255), viz.

$$I(\vec{r},t) \neq \sum_i I_i(\vec{r},t) \tag{1.7}$$

Let us now explore the mathematical formulation of interference (following Wolf 2007, p. 2-4). Consider light vibrations $U_1(t)$ and $U_2(t)$ at two points P_1 and P_2 in a quasi-monochromatic field:

$$U_1(t) = \alpha_1(t) \cdot cos[\phi_1(t) - \bar{\omega}t], \tag{1.8}$$

$$U_2(t) = \alpha_2(t) \cdot cos[\phi(t) - \bar{\omega}t], \tag{1.9}$$

where $\bar{\omega}$ is the mean frequency of the quasi-monochromatic light beams. Suppose that we superpose these vibrations at another point P, the vibrations at this point P are expressed:

$$U(t) = U_1(t) + U_2(t) = \alpha_1(t) \cdot cos[\phi_1(t) - \bar{\omega}t] + \alpha_2(t) \cdot cos[\phi_1(t) - \bar{\omega}t + \delta], \tag{1.10}$$

where δ is the phase difference introduced between the two beams propagating from P_1 to P and from P_2 to P, respectively.

The instantaneous intensity I(t) at the point P may be defined as the square of U(t):

$$I(t) = U^2(t) = I_1(t) + I_2(t) + I_{12}(t), \tag{1.11}$$

where,

$$I_1(t) = \alpha_1^2(t) \cdot cos^2[\phi_1(t) - \bar{\omega}t], \tag{1.12}$$

$$I_2(t) = \alpha_2^2(t) \cdot cos^2[\phi_2(t) - \bar{\omega}t + \delta], \tag{1.13}$$

$$I_{12}(t) = \alpha_1(t)\cdot\alpha_2(t)\cdot\{cos[\phi_1(t)+\phi_2(t)-2\bar{\omega}t+\delta]+cos[\phi_1(t)-\phi_2(t)-\delta]\}. \quad (1.14)$$

Because of the very rapid fluctuations of optical fields, we cannot measure the instantaneous intensity, but only its average over a time interval. By time averaging the above equations, having also assumed that the field amplitudes are effectively time-independent (i.e. $\alpha_1(t)$=α_1, $\alpha_2(t) = \alpha_2 =$ constants), we obtain the following expression for the average intensity at the point of superposition:

$$\langle I_t \rangle = \langle I_1 \rangle_t + \langle I_2 \rangle_t + \langle I_{12} \rangle_t \,, \quad (1.15)$$

with

$$\langle I_1 \rangle_t = \frac{1}{2}\alpha_1^2, \, \langle I_2 \rangle_t = \frac{1}{2}\alpha_2^2, \quad (1.16)$$

$$\langle I_{12} \rangle_t = \alpha_1\alpha_2 \cdot \langle cos\delta\theta \rangle_t \,, \quad (1.17)$$

where

$$\delta\phi = \varphi_1(t) - \varphi_2(t) - \delta \quad (1.18)$$

is the phase difference arising from a combined path length and initial phase-angle difference (Hecht 2017, p. 392)

As may be seen from Eq. 1.15, the average intensity at the point of superposition $\langle I_t \rangle$ is the sum of the averaged intensities $\langle I_1 \rangle_t$ and $\langle I_2 \rangle_t$ of each beam, and of a term, $\langle I_{12} \rangle_t$, which represents the effect of interference between the two beams.

The interference term can also be written in the following equivalent form, combining Eq. 1.16, 1.17:

$$I_{12} = \alpha_1 \cdot \alpha_2 \cdot cos\delta\phi = \sqrt{2I_1} \cdot \sqrt{2I_2} \cdot cos\delta\phi \Rightarrow \quad (1.19)$$

$$I_{12} = 2\sqrt{I_1 I_2} \cdot cos\delta\phi. \quad (1.20)$$

which also stands for I_1, I_2 that are not necessarily equal. Therefore, Eq. 1.15, for the total irradiance at the point of superposition, equivalently reads (Hecht 2017, p. 392):

$$I = I_1 + I_2 + 2\sqrt{I_1 I_2} \cdot cos\delta\phi, \quad (1.21)$$

where, again, all quantities in the above formulas represent time averages.

As we have discussed (Eq. 1.7), light waves exhibit interference when

$$I_{12} \neq 0. \quad (1.22)$$

On the contrary, when $\delta = \pi/2 \Rightarrow cos\delta = 0 \Rightarrow I_{12} = 0 \Rightarrow I = I_1 + I_2$, with the optical disturbances being 90° out-of-phase.

1.3.1 Constructive and Destructive Interference

Based on Eq. 1.21, we conclude that at various points in space, the resultant irradiance can be greater, less than, or equal to $I_1 + I_2$, depending on the value of I_{12}, that is, depending on $\delta\phi$. Let us now investigate the four different possible cases (Hecht 2007, p. 392):

Total Constructive Interference

A maximum irradiance is obtained when $cos\delta\phi = 1$, so that

$$I_{max} = I_1 + I_2 + 2\sqrt{I_1 I_2}, \tag{1.23}$$

when

$$\delta\phi = 0, \pm 2\pi, \pm 4\pi, ... \tag{1.24}$$

In this case of total constructive interference (Fig. 1.1), the phase difference between the two waves is an integer multiple of 2π, and the disturbances are in-phase.

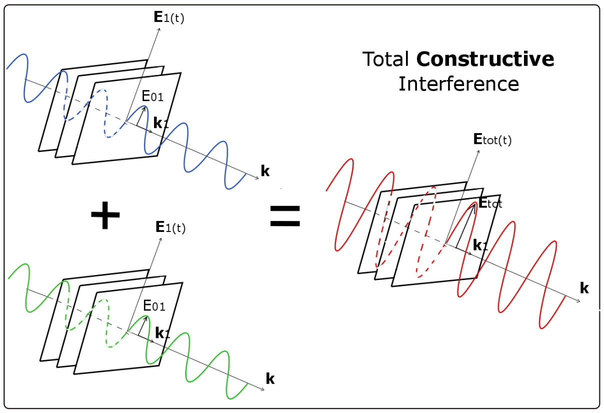

Figure 1.1: Total Constructive Interference.

Constructive Interference

When $0 < cos\delta\phi < 1$, the waves are out-of-phase, and we have the condition of constructive interference: $I_1 + I_2 < I < I_{max}$.

Destructive Interference

For $0 > cos\delta\phi > -1$, we have destructive interference: $I_1 + I_2 > I > I_{min}$.

Total Destructive Interference

A minimum irradiance results when $cos\delta\phi = -1$, the waves are 180° out-of-phase, and troughs overlap crests. Then

$$I_{min} = I_1 + I_2 - 2\sqrt{I_1 I_2}, \tag{1.25}$$

for

$$\delta\phi = \pm\pi, \pm 3\pi, \pm 5\pi, ... \tag{1.26}$$

and we have total destructive interference (Fig. 1.2).

A different, interesting case arises when the irradiance contributions from both sources are equal, i.e. $I_1 = I_2 = I_0$. Then, Eq. 1.21 can be written as

$$I = 2I_0(1 + cos\delta) = 4I_0 \cdot cos^2\frac{\delta\phi}{2}, \tag{1.27}$$

from which it follows that $I_{min} = 0$ and $I_{max} = 4I_0$.

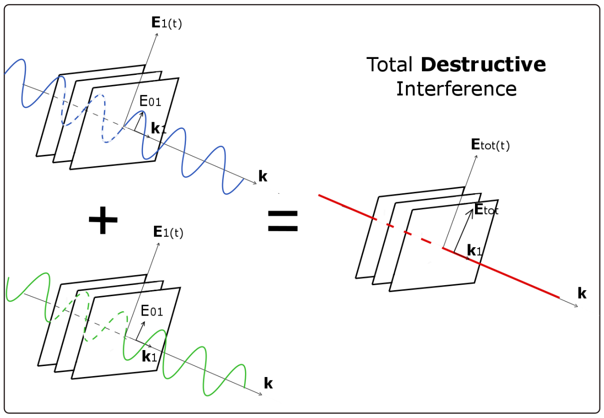

Figure 1.2: Total Destructive Interference.

1.4 Wave coherence

Coherence refers to a wave phase correlation measured at different points; and it is divided into temporal and spatial coherence. Temporal coherence is a measure of the correlation of light wave's phase at different points along the direction of propagation and tells us how monochromatic a source is. Spatial coherence is a measure of the correlation of a light wave's phase at different points transverse to the direction of propagation and tells us how uniform the phase of a wavefront is (Glytsis 2019).

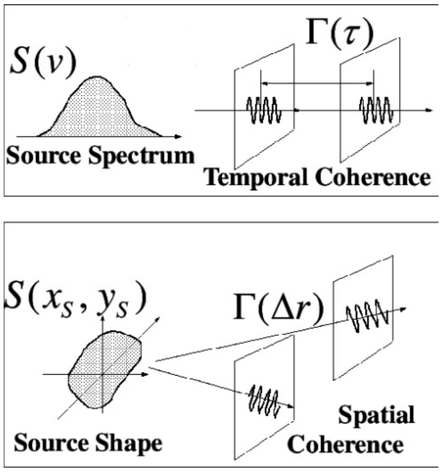

Figure 1.3: Temporal and spatial coherence, (Mitsuo Takeda, Joseph Rosen and Duan Zhihui 2003).

The solutions of the monochromatic wave equation are very useful to describe real light, which is polychromatic. A monochromatic wave has perfect coherence because its phase is completely defined at each and every point in space for all times. If the phase of a monochromatic wave at a space-time point (r_1, t_1) is known, then its phase at any arbitrary space-time point (r_2, t_2) can be precisely determined – in other words, the phases of a monochromatic wave are perfectly correlated.

Just as the phase,so too the amplitude of a monochromatic wave, is perfectly correlated. The extent to which the phase and amplitude correlations in time and space exist, determines the coherence properties of a light wave.

In the context of monochromatic light, we associated coherence with the presence of phase correlations at two space-time locations. However, the common usage of the term coherence is linked with the ability of light to produce interference effects. Within the scope of this interpretation, light is considered coherent if it can produce interference, and incoherent if it cannot. Even if this definition is not precise, it is indubitable the fact that no interference is possible if light is not coherent, but the absence of interference may not necessarily imply incoherence of light.

However, interference fringes are an easily observable manifestation of coherence. If a setup produces fringes, the extant optical field must be coherent, at least to some degree.

The term fringe visibility introduced by Michelson may be more appropriate for a quantitative definition of coherence. Perfect coherence may correspond to 100% visibility and zero visibility may imply complete incoherence – in between we have the regime of the partially coherent light (Sharma 2006, Hecht 2017).

Coherence through the scope of Interference

Light source posses a crucial role in interference phenomena which interferometric systems create. The simplest perfect (single-point source and single wavelength) two-beam interference creates sinusoidal fringes within an almost infinite volume, which are referred to as nonlocalized fringes. However, interference also occurs when broadband light sources are used, like white light-emitting diodes (LEDs), incandescent light bulbs; these are called low coherence sources. By using a broadband source the contrast of the interference fringes decreases, the fringes are limited to smaller volume and are called localized fringes. The amplitude decrease of the fringes is often referred to as a fringe envelope.

Fig. 1.4 shows a comparison of fringe distribution for monochromatic and broadband light sources, which are also called high and low temporal coherence sources. Vertical and horizontal axis correspond to intensity and Optical path difference (OPD) of the interfering waves or beams respectively.

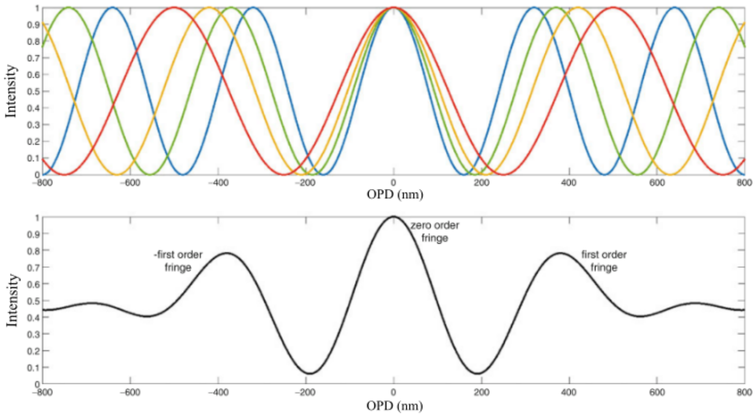

Figure 1.4: Interference fringes: (upper) individual monochromatic fringes for a few single-frequency illuminations and (bottom) white light fringes localized in a smaller space volume (Joanna Schmit, Anna Paluka, 2018).

1.4.1 Temporal coherence

Temporal coherence is intimately related to the frequency bandwidth of a light emitted source. Temporal coherence determines how far two points along the direction of propagation of a wave can be and still possess a definite phase relationship. For that reason, temporal coherence is also called longitudinal coherence. Michelson interferometer, which senses longitudinal path differences between the interfering waves, is ideally suited for investigating temporal coherence of light fields.

The main measure of temporal coherence, describing the extent of time for which the optical field fluctuates in unison at two instants of time, is a normalized autocorrelation function, also called complex degree of temporal coherence or gamma coherence function which reads the Eq. 1.28.

$$\gamma(\tau) = \frac{\langle E^{*}(t) \cdot E(t+\tau)\rangle}{\langle E^{*}(t) \cdot E(t)\rangle} \tag{1.28}$$

,

where $E^{*}(t)$ is a field conjugate to E(t) and τ is the time delay between field $E^{*}(t)$ and its delayed replica E(t+τ).

The coherence function value carries information about the degree of correlation between E(t) and E(t+τ), whose fields in practice have to originate from the same source point; otherwise, there is zero correlation. The value of the complex degree of temporal coherence function cannot exceed unity, as shown in Eq. 1.29

$$0 \leq |\gamma(\tau)| \leq 1 \tag{1.29}$$

The time delay for which $|\gamma(\tau)|$ drops to 1/2 or 1/e is referred to as coherence time τ_c. Coherence time is the power-equivalent width of a coherence function, as shown in Eq. 1.30.

$$\tau_c = \int_{-\infty}^{-\infty} |\gamma(\tau)|^2 d\tau \tag{1.30}$$

The dependence between the coherence function and coherence time is shown in Fig. 1.5.

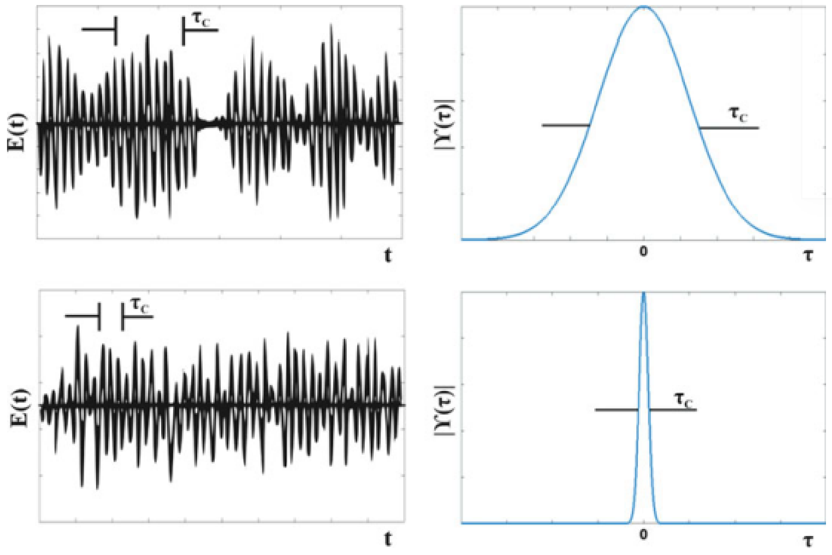

Figure 1.5: The dependence between the coherence function and coherence time (Joanna Schmit, Anna Paluka, 2018).

Thus, the source of radiation can be characterized by the coherence time τ_c or its equivalent coherence length l_c = cτ_c, where c is the speed of light. A monochromatic light source of single angular frequency ω_0 and single wavelength λ_0 , ω_0=2π ν_0, where frequency ν_0=c/λ_0) can be characterized by a complex degree of temporal coherence equal to $\gamma(\tau)$=exp(iω_0 τ) and $|\gamma(\tau)|$= 1 for all τ. If no other factors occur, then using such light will result in interference fringes of highest visibility regardless of time delay. On the other hand, if incoherent light is used, then only for τ=0, the complex degree can reach maximum and $|\gamma(0)|$=1. Those two extreme problems are only theoretical and in practice the cases in between only should be taken into consideration.

The gamma coherence function is related to the source spectrum S by Fourier transform according to the Wiener – Khinchin theorem (Mandel and Wolf 1995), as shown in Eq.1.31

$$S(\omega) = \int_{-\infty}^{-\infty} \gamma \cdot exp(-i2\pi\omega\tau)d\tau \tag{1.31}$$

The relation is shown in Fig. 1.6. The light of broad spectral range has a short coherence time, while a narrow band light source has longer coherence time. For monochromatic light, the spectrum consists of a single frequency S(ω) = δ(ω-ω_0) and τ_c=∞ , Δ ω=0. Light with broader spectrum for which $0 < \tau_c < 1$ is considered as temporarily partially coherent.

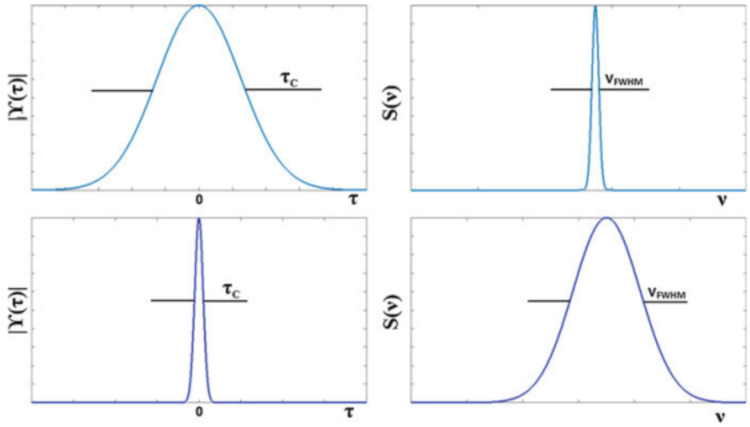

Figure 1.6: The dependence between the spectral range and coherence time (Joanna Schmit, Anna Paluka, 2018).

The most common definition of spectral width or linewidth Δ ω_c of the source spectrum range is the full width at half maximum value (FWHM); however, generally spectral width can be derived from Eq. 1.32 which also takes into account the shape of the spectrum profile S(ω) as they can be different for different sources.

$$\Delta\omega_c = \frac{(\int_0^\infty S(\omega)d\omega)^2}{\int_0^\infty S^2(\omega)d\omega} \tag{1.32}$$

1.4.2 Spatial coherence

Spatial coherence of light determines how far two points can lie in a plane transverse to the direction of propagation of light and still be correlated in phase. Utilizing interferometers of the type used by Young in his famous two-slit interference experiment, spatial coherence can be investigated .

Spatial coherence of light depends on the physical size of the light source. Light coming from a point source, has a high degree of spatial coherence, irrespective of the frequency bandwidth of the source. Commonly observed speckles with laser light reflect a high degree of spatial coherence of laser light despite the laser not being a point source. Light from an extended source, on the other hand, has considerably lower spatial coherence because different points of the extended source radiate independently and therefore are mutually incoherent.

We will now develop a mathematical framework to characterize the coherence of light fields. Again for the analysis of spatial coherence effects, they are considered two optical field disturbances E(r_1,t) and E(r_2, t+τ) originating in two different points in space. The complex degree of coherence is given in Eq. 1.33, and indicates a cross-correlation coefficient that shows the degree of correlation between those disturbances.

$$\gamma(r_1, r_2, \tau) = \frac{\langle E^*(r_1, t) \cdot E(r_2, t+\tau)\rangle}{\sqrt{I(r_1) \cdot I(r_2)}} \tag{1.33}$$

,

where $I(r_1)$, $I(r_2)$ are the intensities at points r_1, r_2 respectively. Allow us to remind the quantities $I_{1,2}$=⟨|Eˆ2˙1,2|⟩

The absolute value of the complex degree of coherence can not exceed unity, as shown in Eq. 1.34

$$0 \leq |\gamma(r_1, r_2, \tau)| \leq 1 \tag{1.34}$$

For zero-time delay, $\tau = 0$, between the optical fields, the complex degree of coherence refers only to their position in space and is the measure of the degree of spatial coherence. If the degree of spatial coherence equals zero, the field disturbances at r_1 and r_2 are uncorrelated, while if the degree equals unity, then the fields are considered fully correlated. In practice, light coming from a point source is treated as spatially coherent; whereas, for extended light sources, its size determines the degree of the coherence. Assuming that time delay $\tau = 0$ and the OPD is much shorter than the coherence length l_c = cτ_c, the light can be treated as monochromatic. In this case, a complex degree of coherence, as described by Eq. 1.35, is called normalized mutual intensity and describes the spatial coherence completely.

$$\gamma(r_1, r_2) = \frac{\langle E^*(r_1, t) \cdot E(r_2, t)\rangle}{\sqrt{I(r_1) \cdot I(r_2)}} \tag{1.35}$$

As in previous cases, Eq. 1.29 and Eq.1.34, the value of normalized mutual intensity is between zero and unity. The value $\mid \gamma(r_1,r_2)\mid = 1$ shows the complete correlation of the optical field in r_1 and r_2 , while $\mid \gamma(r_1,r_2)\mid = 0$ states otherwise. When discussing spatial coherence, it is not possible to omit the subject of coherence area, which is in the vicinity of r_1 for which the function $\mid \gamma(r_1,r_2)\mid$ is greater than 1/2 or 1/e. The coherence area is very important while characterizing random light, especially for describing its relation to the optical system. For example, if the area of coherence is greater than optical system's aperture ($\mid \gamma(r_1,r_2)\mid \approx 1$ at all points), the light is considered coherent; otherwise, it is considered as spatially partially coherent.

Chapter 2

Introduction to Profilometry

2.1 Overview of Profilometry Techniques

This section introduces some of the concepts used in the measurement and characterization of surface texture. Techniques used in surface metrology can broadly be classified used into two categories, contact and non-contact. Non-contact techniques can be again subdivided into non-optical and optical categories depending upon the method of instrumentation, as shown in Fig. 2.1

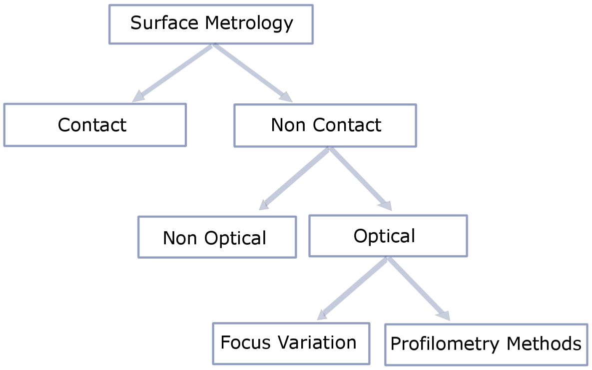

Figure 2.1: Surface Metrology Techniques.

2.1.1 Contact Profilometry

Contact profilometry is exclusively related to the fact that there has to be contact with the sample. The most representative example of these profilometers are known as Stylus profilometers.

Stylus Profilometer

Stylus profilometers use a probe to detect the surface, physically moving a probe along the surface in order to acquire the surface height. This is done mechanically with a feedback loop that monitors the force from the sample pushing up against the probe as it scans along the surface. A feedback system is used to keep the arm with a specific amount of torque on it, known as the "setpoint". The height position of the diamond stylus generates an analog signal which is converted into a digital signal, stored, analyzed, and displayed. The changes in the Z position of the arm holder can then be used to reconstruct the surface. A schematic representation of Stylus profilometer is shown in Fig. 2.2. Typically Characteristics of a Stylus profilometer are the needle size, 2μm diameter, the tip load which is o the order of pico-Newton and accuracy considered close to 1 nm. A typical profilometer can measure small vertical features ranging in height from 10 nanometres to some micrometers.

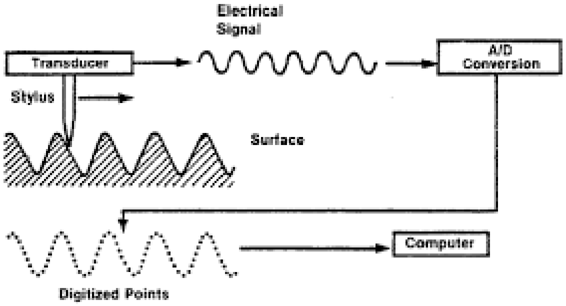

Figure 2.2: Schematic representation of a Stylus profilometer (Muhammad Rizwan Amirzada, 2014).

Stylus technique offers great accuracy and provide the ability to measure the profile of a very long line with one measurement. The drawback of this technique is mainly that this is a method that requires contact with the sample, so it is very possible the sample surface to be damaged after the measurement. This is the reason why a Stylus profilometer cannot be used at soft specimens such as tissues and other biological materials. More importantly, it measures a one dimensional (1D) surface profile, which is time-consuming, if surface height maps need to be recorded (D.J. Whitehouse 2011, R. K. Leach 2010).

Atomic Force Microscopy (AFM)

In atomic force microscopy technique (AFM), the interaction between the probe and the surface, is include attractive and repulsive forces. Vertical resolution can be less than a nanometre and different types of probes are used depending upon the measurement needs (G. Binnig and C. F. Quate).

2.1.2 Non Contact Profilometry

In non-contact profilometry, electromagnetic radiation (such as light or X-ray) is used illuminating the sample, its response is collected by a detector. By analyzing and characterizing its response, the information about the surface morphology is retrieved.

Non-contact topography measurement can also be sub-classified into: non-optical and optical. Four of non-optical techniques electron microscopy (EM) and X-ray topography (XRT), Scanning Tunneling Microscopy (STM), Scanning Probe Microscopy (SPM) and Near-field Scanning Optical Microscopy (NSOM) are described here.

Non-Optical Measurement Techniques

SEM

Both, scanning electron microscopy (SEM) and transmission electron microscope (TEM) belong to the same category of electron microscopy. The most representative technique in surface characterization used to be SEM. The scanning electron microscope (SEM) uses a focused beam of high-energy electrons to generate a variety of signals at the surface of the specimens. The signals that derive from electron-sample interactions reveal information about the sample surface, chemical composition, and crystalline structure and orientation of materials making up the sample. Usually, data are collected from a selected area of the sample's surface, and a 2-dimensional image is generated that presents the spatial variations of the sample surface. Areas ranging from approximately 5 μm to 1 cm in width can be imaged with the spatial resolution to be 50 to 100 nm (Susan Swapp, University of Wyoming).

XRD

In XRD technique, a collimated beam of X-rays incidents the surface under test, generating different diffracted patterns which depend on the surface microstructure. From these patterns, surface topography is computed. XRD works best for simple structures. The main advantage of this technique is potentially high resolution 3D images. (D. R. Black and G. G. Long, 2004).

STM

A sharp conducting tip traverses the sample surface in STM technique. A bias voltage is applied between the tip and the surface and the electrical interaction between them is acquired. The tip traverses the sample and electrons from the surface tunnel through to the tip, according to the phenomenon known as quantum mechanical tunneling. This technique offers high vertical resolution in surface profiling but only small areas of the surface can be measured since the range of scan is about hundreds of microns (G. Binnig and H. Rohrer).

SPM

In SPM technique, is used a tiny probe which moves relative to the surface staying very close to it. The kind of interactions which take place between the probe and the surface during this movement are mainly electrical, attractive interactions, repulsive forces etc. These interactions are recorded, being analyzed in order to exact the profile measurement (R. K. Leach 2010, G. Binnig and H. Rohrer).

NSOM

Near-field scanning optical microscopy technique uses a tiny tip, of bottom diameter of the order some nanometres. Through this tip, the surface is illuminated and the scattered light from the surface is collected. The emission of the light is very close to the surface. The distance between the tip and the surface must remain less than the tip diameter to obtain images of the surface with sub-wavelength resolution (E. Betzig and J. K. Trautman).

Optical Measurement Techniques

The optical measurements techniques are exclusively based on optical contact with the under test sample surface. Different optical measurement techniques such as focus variation (FV), are used for surface topography. In all of these cases, either narrowband sources such as lasers or broadband sources such as LED are used for illumination. Imaging and interferometric systems are used for these techniques, for recording images or video of the surface. After that, different computation algorithms are applied to the data to extract different parameters related to surface metrology.

Confocal Scanning Microscopy (CSM)

Scanning confocal microscopes employ a pair of pinhole apertures to eliminate light from the non-focused points of the object, limiting the specimen focal plane to a confined volume. The purpose of the method is to find the optimum focus level of one microscope on the sample while the position of an objective lens changes, by using piezoelectric crystal (PZT). During the movement, the intensity of the reflected radiation fluctuates, and maximizes right on the focus. So by applying the above for all points of the sample, we can find the surface profile. In the following figure (Fig. 2.3) is represented a schematic of the confocal microscope principle.

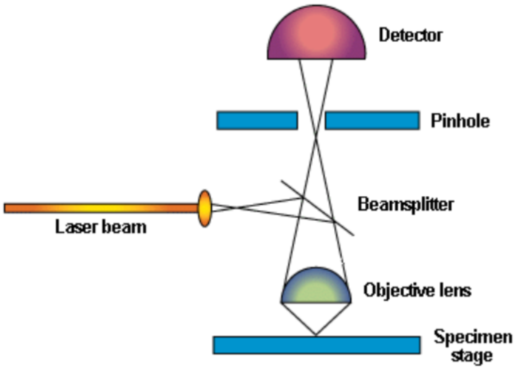

Figure 2.3: Schematic representation of the confocal microscope principle,retrieved from: notes of Confocal laser scanning microscopy, University of Cape Town (Laura Takkunen et.al. 2014).

The advantages of this technique are that it is applicable to live specimens, therefore suitable for medical applications, is commercially available, easy to use, it can be implemented on low-cost systems and provides a great field of view. The disadvantage is related with the resolution, it has a resolution dependent on the numerical aperture (NA) of the objective lens and the sampling length of the filter used which provides, typically, a lateral resolution is of the order of 2 μm and a vertical resolution of the order of 50 nm.

Interferometry based Methods

Phase Shifting Interferometry (PSI)

Phase shifting interferometers (PSI) are used to obtain fast, three-dimensional profiles of surfaces with vertical and lateral resolution of the order of a nanometre. In this technique, phase retrieval involves sequential shifting of the optical path of the one interferometer arm (reference arm) relative to the other arm (sample arm) by a number of predefined phase steps. By analyzing the resulting interference pattern a wrapped phase-map arises. By applying phase unwrapping. This device is typically limited to measurements of smooth and continuous surfaces. Surfaces which introduce a phase shift larger than 2π between adjacent points result in phase ambiguity errors. PSI has nanometre resolution and accuracy, but the height measurement values are limited to within a half of the wavelength, since the integer part of the fringe order cannot be determined, In reality we cannot distinguish whether the difference in height between two points is α, $\alpha + \lambda \ / \ 2$, $\alpha + 2\lambda \ / \ 2$, $\alpha + 3\lambda \ / \ 2$, etc. When rougher surfaces are measured, severe errors can arise. This fact is exclusively related with the laser high coherence length (Dai Xiaoli, Seta Katuo, 1998, Zygo Corp, Kanik

Palodhi, 2013).

White Light Scanning Interferometry

White light scanning interferometry (WLSI) is a useful technique to measure surface profile when a sample under test contains discontinuous structures. Scanning is realized using a micromovement component e.g a piezoelectric actuator. A black and white CCD camera is usually utilized to capture multiple interferograms, which then after numerical processing are used to retrieve the profile measurement, mainly, by detecting the peak position of the coherence envelope. This is possible since the fringe visibility is maximal when the optical path difference (OPD) between the sample and reference beam is zero. This procedure is repeated for each pixel, as many times as the steps of the micromovement component are. The measuring range on the vertical axis depends on the micro-movement component characteristics, since it is equal to its maximum displacement range. A typical value of a piezoelectric actuator maximum displacement, and thus the height value range is $10 - 100\mu$m. The vertical resolution of white light scanning interferometers can reach the order of a nanometer (Suodong Ma et.al. 2011).

Spectrally Resolved White Light Profilometry (SRWLI)

The technique of surface profile measurement utilizing white light interferometry (WLI) is widely used in industry as a non-contact, non-destructive method to quickly and accurately measure the profile of microscopic surfaces.

The system developed in this thesis is based on the spectrally resolved white light profilometry (SRWLI) technique and measures the profile of a line of our sample. Spectrally resolved white-light interferometry is a technique that analyses the spectrum of the interference pattern that is formed when a sample located at the one arm of an interferometer and is illuminated with a broadband light source. The interferogram, which is recorded by a CCD camera, encorporates the phase as a function of wavenumber. SRWLI is useful as a profilometry tool when dealing with rough sample surfaces which present abrupt height variations. In these cases, the usual monochromatic phase-shifting interferometry (PSI) cannot be applied due to ambiguity problems in the phase unwrapping process.

SRWLI measures one line of a sample surface and so it is deteriorating in relation to the surface measuring techniques, however, these techniques, require a large number of interfetograms to be processed and, consequently, this data analysis seems to be slower enough comparing with our technique. In this method, optical phase can be obtained in an absolute way, without the use of optical path difference modulators i.e. scanning can be completely avoided.

The measuring rate is limited only by the camera frame rate. Typically, time between two consecutive measurements can be in the order of 16 msec. Very short measurment duration can be achieved using a single shot illumination source. Due to use of an optical method, the high speed efficiency, and the vertical resolution of a few nanometres (10 nm), this method is very promising for sample measurements that change their profile over time (Patrick Sandoz Gilbert Tribillon, 1993, Petr Hlubina et.al. 2003).

2.2 Interferometry

Interferometry is a well-known measurement technique which uses electromagnetic waves that superpose and interfere, in order to study their resulting interference pattern (fringes) and thus estimate their phase difference. From the metrology point of view, this information is very useful since from it we can extract the surface profile, its roughness, its thickness, measure small displacements, and refractive index changes etc. The instrument that realizes this technique is known as an interferometer.

2.2.1 Interferometers

Interference, experimentally occurs using interferometers, with the most important amplitude-splitting interferometers to be Michelson, Mirau and Linnik like interferometers. In each of the above, light from a source is divided into two beams with the help of a beam splitter, and then the two beams follow different path lengths and eventually meet up again and superimpose. For the shake of simplicity, we assume that the initial beam is a quasi monochromatic wave. Let us note here, that amplitude-splitting interferometers are associated with the fact that the transmitted and reflected waves are exact replicas of the original wavefront, thus in that sense, the amplitude has been ”split”.

Michelson Interferometer

The Michelson interferometer was introduced by Abraham Michelson at the end of the 19^{th} century and is probably the most representative of the the rest due to the simplicity of its setup as well as the relative ease its implementation (Hecht, 2002). In Fig.2.4 is represented a typical Michelson interferometer.

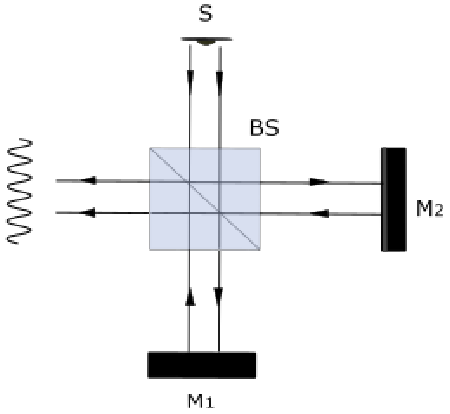

Figure 2.4: Schematic of a Michelson interferometer. S light source, M_1, M_2 mirrors, BS beam splitter. At the exit is the intensity profile of the interference is depicted

The initial light beam which is emitted from a source S, meets a beam splitter, and is splitted into two equal halves beams. Each of the two beams propagate and is reflected from the mirrors M_1 and M_2. When they reach the beam splitter again, the two beams reconstitute and contribute with each passing a different one optical path length. By changing the position of one mirror, we can change the OPD of the beams having different interference patterns formed.

Mirau Interferometer

The Mirau interferometer was introduced, later than the Michelson interferometer, by André Henri Mirau who received a Patent for it in 1949. In fact, it is an interferometer which looks like a Michelson, folded on a single axis. A schematic representation is shown in the figure below (Fig. 2.5):

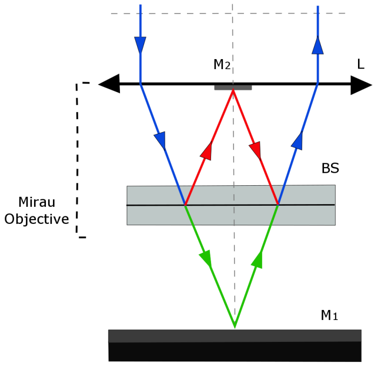

Figure 2.5: Schematic representation of a Mirau interferometer. L lens, M_1, M_2 mirrors, BS beam splitter.

The interferometer is comprised of a focusing lens of focal length f, which on its flat side is mounted a small mirror. In addition there is a beam splitter situated at distance $f/2$ away from the lens. The whole system is aligned with the beam propagation axis, as shown in the figure. These optical parts constitute the Mirau Objective which can be treated as a single optical component. A second mirror is positioned at distance $f/2$ from the Mirau objective. The principle of operation is as follows: Light emitted from the source, enters the interferometer and is focused by the lens L on the big mirror M_1. During this path, part of the beam (red line) is reflected from the beam splitter backwards and strikes the small mirror M_2 placed on the lens. The mirror M_2, again reflects the beam forward in order to be reflected back by beam splitter and return to the source direction. The other part of the beam (green line) which was not reflected during the initial incidence on the beam splitter, is focused on the mirror M_1 and is reflected back to the beam splitter. At this point, on the beam splitter, the two beams contribute. Using a second beam splitter, before Mirau Objective (which does not appear in the figure) we can direct the final contributing beam to a detector. By changing the position of one mirror (in this case the big one), we can change the OPD of the two beams resulting different interference fringes distributions.

Linnik Interferometer

The principle of Linnik interferometer was presente in a paper by W. P. Linnik published in 1933. The basic arrangement of the Linnik interferometer comprising a light source, a collimator, a beam-splitting prism, uniform objective lenses with completely identical optical distances, a specimen surface, which gives rise to an image, and a reference mirror, which gives rise to a reflection image. A schematic representation is given in Fig. 2.6 where, the sample surface is replaced by a second mirror.

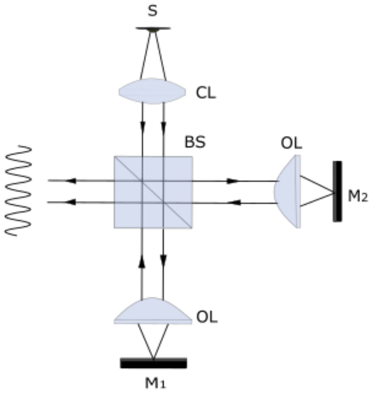

Figure 2.6: Schematic representation of a Linnik interferometer. CL collimator lens, M_1, M_2 mirrors, OL objective lens, BS beam splitter and at the exit is an intensity profile of the interference beam.

The beam propagation in Linnik interferometer is the following: The initial light beam which is emitted from a source S, is being collimated by the collimator lens CL, meets a beam splitter, and is splitted into two beams which are now traveling perpendicular to each other. Both beams propagate and are focused by the two identical objective lenses OL on the mirrors M_1 and M_2 plane. Then, they are reflected backwards and are being collimated by the lenses OL. At the beam splitter, the beams meet up again, contributing each other.

Chapter 3

Spectral Interference Fringes

Let us now study the effect of wave interference in the spectrum of broadband white light sources. Using a Michelson inteferometer setup, in (Fig. 3.1) we see our initial white light which is splitted into two equal halves. Both beams are reflected and return back to the beam splitter where they interfere having traveled different optical path lengths L_1 and L_2.

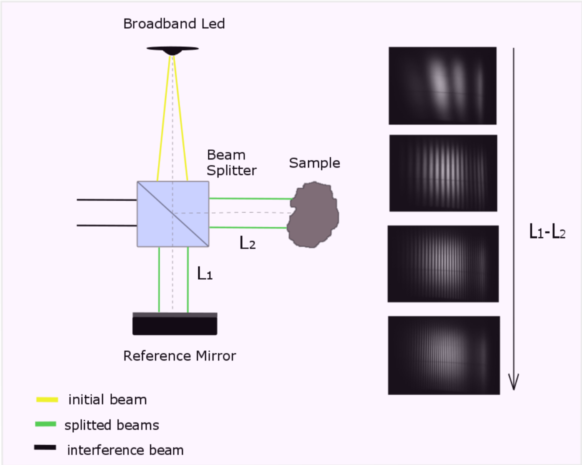

Figure 3.1: Michelson interferometer and interference fringes variation as a function of OPD ($L_1 - L_2$) change. The initial beam (yellow) is splitted into two beams (green) which are both reflected, meet up and interfere (black beam). On the right side of the figure, we can see four images of spectral interference fringes which are captured from the camera. By moving the reference mirror, the OPD ($L_1 - L_2$) of the beams increases resulting in a variation of the spectral fringes distribution.

We can see in Fig.3.1 the optical path lengths L_1 and L_2 which correspond to our beams. Increasing or decreasing the optical path L_1 by moving the reference mirror, we change the OPD ($= L_1 - L_2$) between the beams, resulting in a variation in the distribution of interference fringes. Using numerical simulations we can visualize the effect of superposition in the spectral domain. Increasing the OPD, the density of interference fringes increases (see Fig. reffig˙OPD). At a single point $P = (x, y)$ in the outpout of the interferometer the intensity is described by:

$$I(P,\lambda) = I_1(P,\lambda) + I_2(P,\lambda) + 2\sqrt{I_1(P,\lambda)I_2(P,\lambda)}\cos(\frac{2\pi}{\lambda}OPD) \tag{3.1}$$

The resulting modulation of the spectral intensity for various OPD values (estimated from Eq. 3.1 using wxMaxima) is shown in Fig. 3.2, where the spectral intensity is plotted as a function of the wavelength. The red curve represents the fringes modulation, while the black curve the normalized source spectral distribution. Clearly, by increasing the OPD, the phase of the cosine term variates, see Eq. 3.1, resulting the modulation of intensity.

At zero OPD, the spectral intensity distribution is identical with the source intensity distribution. As the OPD is increased, the initial spectrum is modulated by an increasing number of spectral interference fringes.

As the OPD value is increased, the density of the spectral fringes is such so that fringes appear less and less distinguishable.

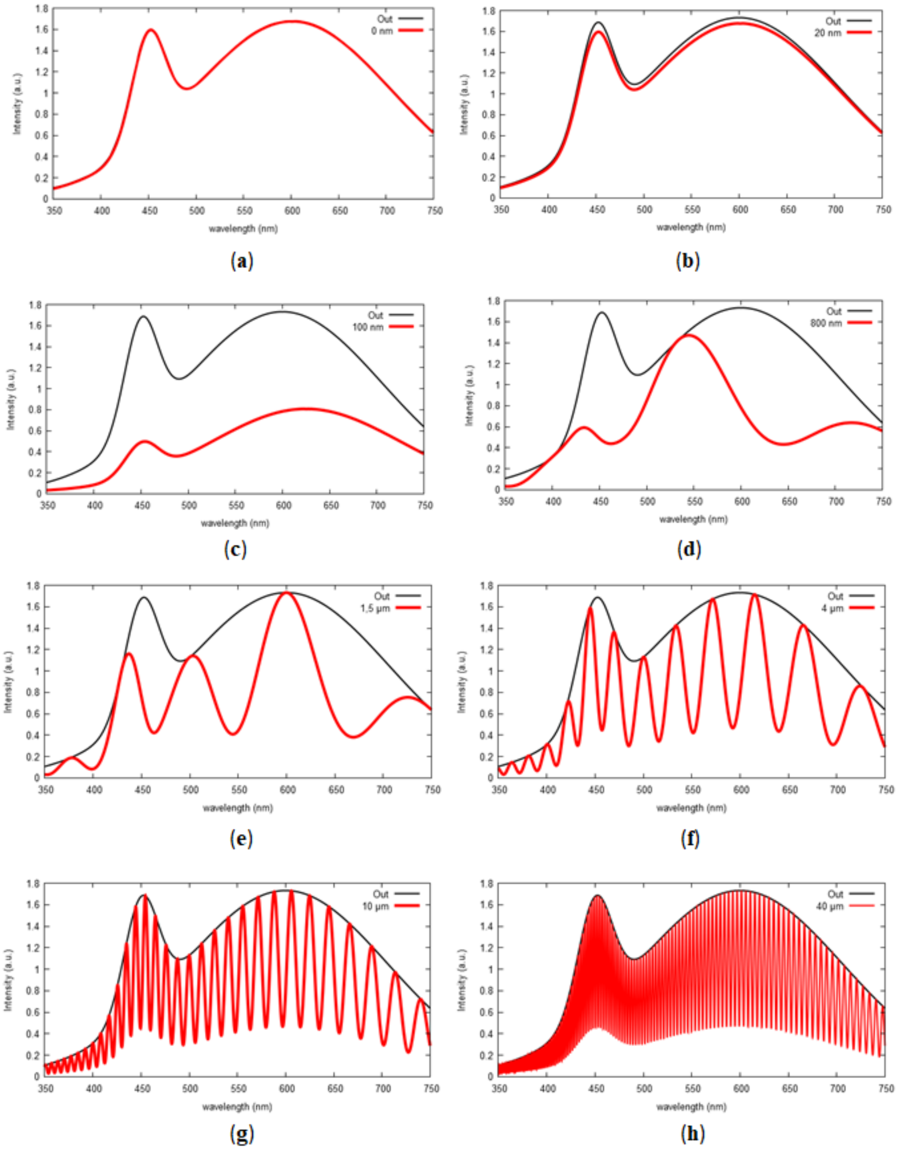

(a) (b) (c) (d) (e) (f) (g) (h)

Figure 3.2: Intensity modulation for different OPD values.(a):OPD=0nm, (b):OPD=20 nm, (c):OPD=100 nm, (d):OPD=800 nm, (e):OPD=1.5 μm, (f):OPD=4 μm, (g):OPD=10 μm, (h):OPD=40 μm

Chapter 4

Experimental Setup: Profilometry Device

A spectral interferometer profilometry device was designed and implemented. This white light profilemeter (i.e. operates with a white light broadband source), based on a Michelson interferometer configuration, is shown in Fig. 4.1 while in Fig.4.2 is shown an image of the laboratory prototype device.

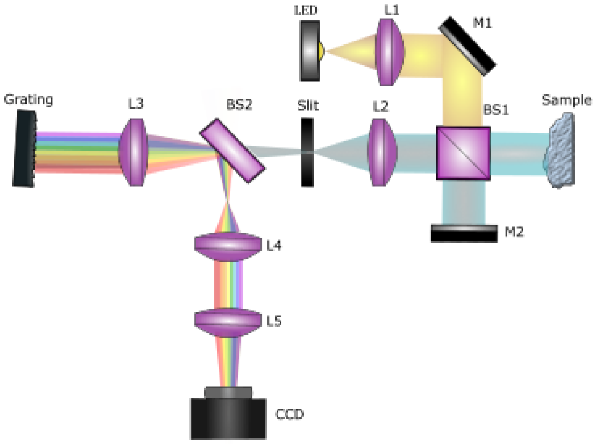

Figure 4.1: Schematic representation of the experimental setup based on Michelson interferometer. Abbreviations, as met by the light beam: L: lens, M: mirror, BS: beam splitter, CCD: charge coupled device.

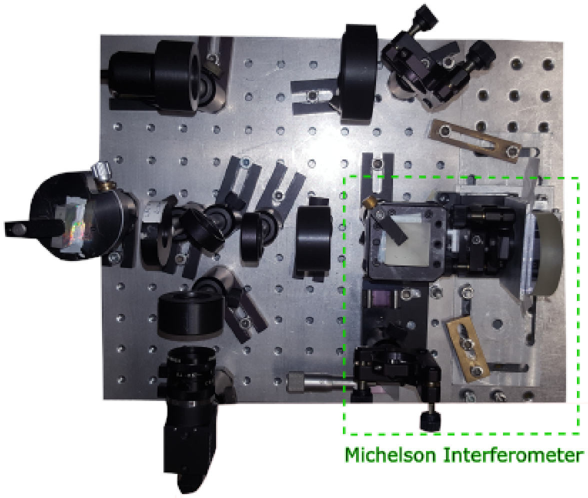

Figure 4.2: Top view photo of the experimental setup based on Michelson interferometer.

By using this setup (Fig. 4.2) which is based on Michelson interferometer, there were difficulties in measuring low reflectivity and/or rough samples. For this reason, this setup was replaced by an implementation of a Linnik interferometer based on its suitability for measuring the surface profile of samples characterized by roughness or low reflectivity.

Let us note here, that using this implementation, beam alignment was a difficult procedure due to the strick nature of the white light interference condition (spatial coherence of the order of 1 μm).

The interferometer profilometry device based on a Linnik interferometer configuration, is shown in Fig. 4.3 while in Fig.4.4 is shown an image of the laboratory prototype device.

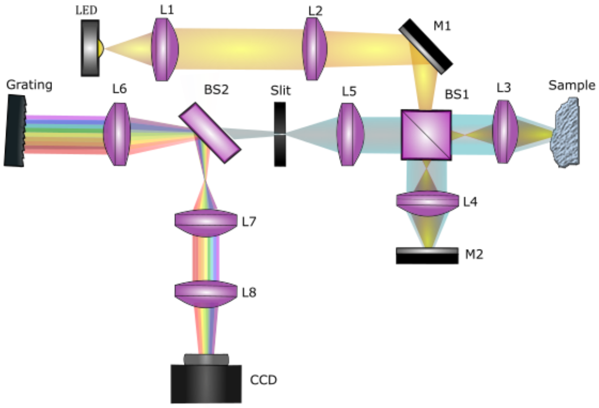

Figure 4.3: Schematic representation of the experimental setup. Abbreviations, as met by the light beam: L: lens, M: mirror, BS: beam splitter, CCD: charge coupled device.

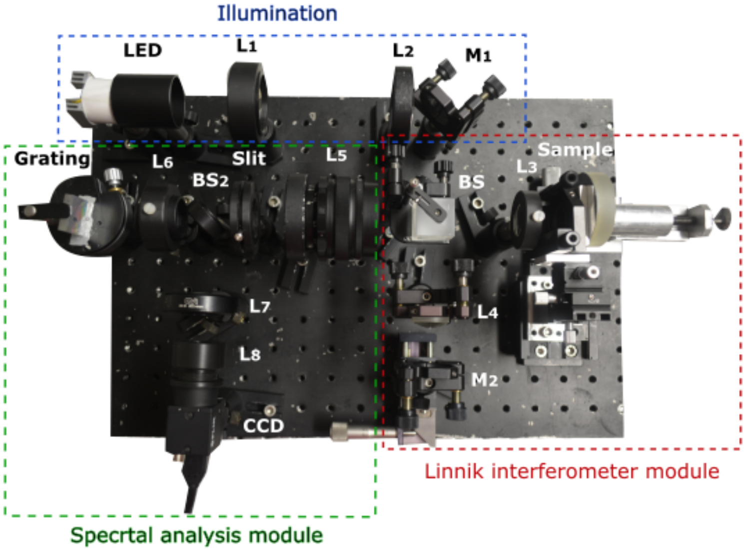

Figure 4.4: Photo of the experimental setup in laboratory.

As we can see here (Fig. 4.3), an objective lens L_3 is placed between the sample and the BS, as close to the sample as possible, allowing the increase of the angle range over which the system can accept light, i.e. the numerical aperture (NA) of the system. Indeed by implementing the Linnik scheme, the NA of our system was increased by a factor of 4x increasing, from 0.1 to 0.4.

In Fig.4.5, is shown a schematic representation of the two interferometer configurations, Michelson and Linnik configuration and the qualitative light collection angles in each case.

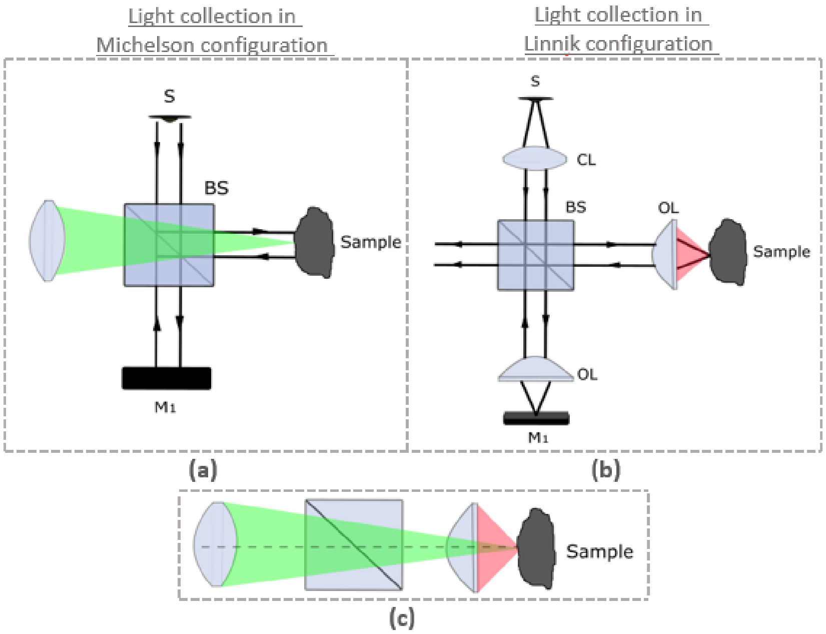

Figure 4.5: Light collection in Michelson and in Linnik interferometer configuration. (a): portion of collected light in Michelson interferometer configuration (green beam), (b): portion of collected light in Linnik interferometer configuration (pink beam), (c): collected portions of light in both cases, green refers to Michelson and pink to Linnik configuration.

We can clearly see that the portion of collected light is greater in the case of Linnik interferometer configuration than this in Michelson configuration and therefore, the NA of the system increases. Let us now, compare the result of this NA increase. The signal level which both setups accept from a rough sample is captured by the CCD camera of the device and its intensity profile is shown in Fig. 4.6 and Fig.4.7. Let us also note, that due to the low signal to noise ratio, this sample could not be measured using Michelson interferometer configuration.

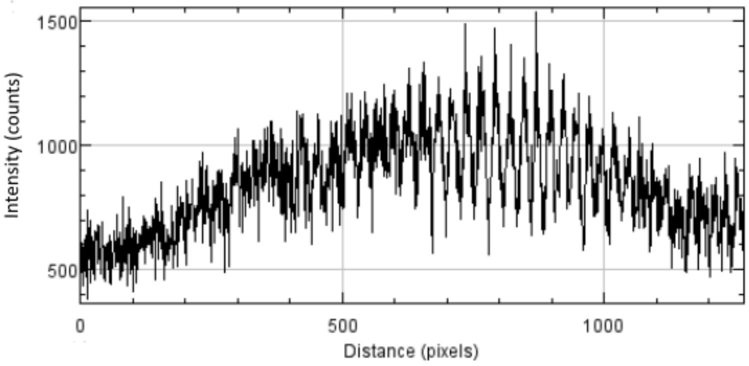

Figure 4.6: Intensity profile of a rough sample using Michelson interferometer implementation in our setup.

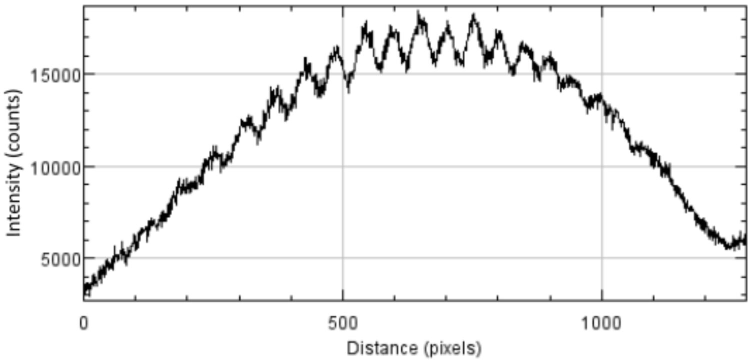

Figure 4.7: Intensity profile of a rough sample using Linnik interferometer implementation in our setup.

As we can see in the above figures the signal is dramatically increased in absulute values (10x). Clearly, such samples can be measured by using the Linnik interferometer implementation.
We shall now describe our device, focusing on the three major components that constitute the setup, namely: 1. Illumination, 2. the Linnik interferometer module, and 3. specrtal analysis module.

Illumination

The light source is comprised by a white light broadband light-emitting diode (LED) with 400-800 nm emission spectrum (Fig. 4.8), and 2 W maximum emission.

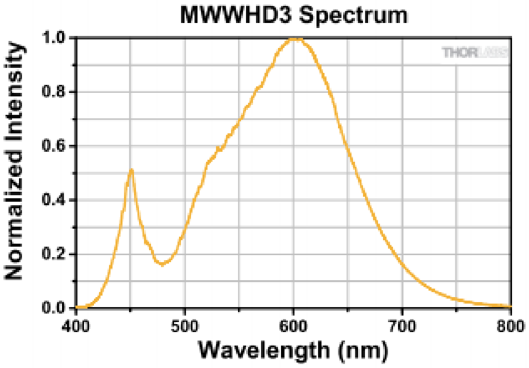

Figure 4.8: Typical spectrum of the emission of LED source.

A schematic representation of the light source component is shown in Fig. 4.9. The light beam emitted from the LED is collimated by a lens (L_1, with 50mm focal length, 25,4 mm diameter). Then, a convex lens (L_2, with 100 mm focal length, 35 mm diameter) focuses the beam, and an aluminum mirror (M1, with 25,4 mm diameter) at 45° directs it towards the beam splitter.

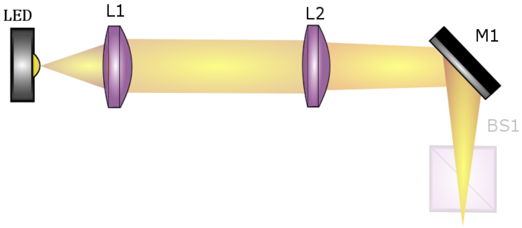

Figure 4.9: Schematic representation of the illumination module. Abbreviations, as met by the light beam: L: lens, M: mirror, BS: beam splitter.

Linnik interferometer module

The role of the inteferometer component in the profilometry setup is critical: the two recombining light beams have a phase difference which produces interference fringes. The exact pattern of interference depends on the optical path difference of the sample reflected beam. This optical path difference is very sensitive to the surface profile of the sample of interest, allowing us to optically characterize its surface topology.

After being reflected by the mirror M_1, the light enters a Linnik interferometer (Fig. 4.10). A beam splitter (BS) splits the beam into two halves of equal intensity (the reflected and the transmitted), which are then focused by two identical convergent lenses (L_3, L_4, with 30 mm focal length), onto the sample and the reference mirror (M_2), respectively. The two beams are back-reflected and recombined at the beam splitter, where they overlap and interfere.

It should be noted that when the beams recombine, they are collimated, since the two convergent lenses are placed at distances equal to their focal length, from the sample and mirror.

It is worth mentioning that the choice of the Linnik interferometer implementation was decided for a specific reason. The Michelson interferometer implementation had preceded the Linnik interferometer in our setup since it is more trivial to build. The reason of this replacement, was the disability of measuring rough surface samples. The inadequate signal collection of samples which are rough or present low reflectivity, set their surface measurement impossible. This problem was resolved by situating an objective lens between the sample and the BS as close to the sample as it could be, (see Fig. 4.10). This results in the increase of the range of angles over which the system can accept light, i.e. the numerical aperture (NA) of our system. By implementing Linnik interferometer, the NA of our system went out from 0.1 to 0.4, is increased fourfold. The realization of white light interference required the placement of an identical lens to the other arm too, which finally results in a Linnik interferometer implementation.

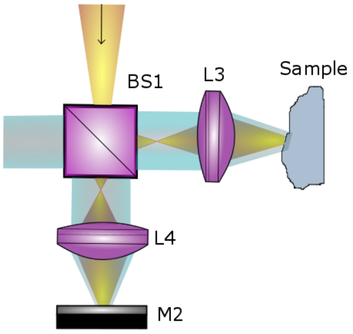

Figure 4.10: Schematic representation of the Linnik interferometer component. BS beam splitter, L lens, M mirror. Yellow denotes the illumination beam while blue denotes reflected light that is collected by the interferometrer.

Let us mention here that due to difficulties in alignment, a special sample holder was designed. This holder achieves to position any flat sample at the same distance from the beamsplitter, interpedently from its thickness. Furthermore, the sample is easily placed and removed from the holder by using a retractable,spring loaded, constant force clamp on the back surface of the sample. As shown in Fig.4.11.

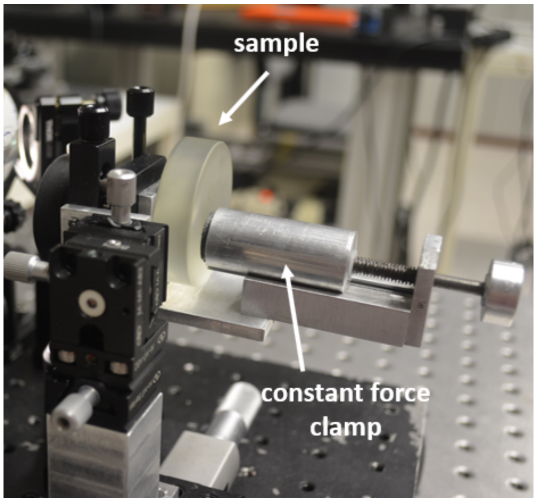

Figure 4.11: Sample holder.

Spectral analysis module

The Specrtal analysis module is depicted in Fig. 4.12, and it consists of the following optical elements: four focusing lenses, a slit (20 μm width, 3 mm height), a beam splitter plate, a grating (600 grooves/mm, reflective diffraction blazed), and a charge coupled device (CCD) camera (1280×1024 pixels, 6.1mm $\times$ 4.9mm sensor size), connected with a computer.

The four lenses include a photographic lens (L5, with 48 mm focal length), an achromatic pair of lenses (L6 with 100 mm total focal length), and two doublet lenses (L7, L8, with 25,4 mm diameter, and focal lengths of 30mm and 50mm, respectively).

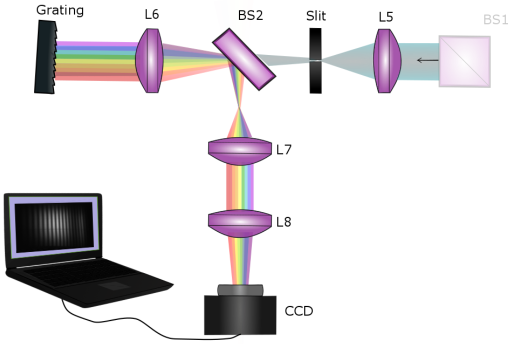

Figure 4.12: Schematic representation of the specrtal analysis module. BS beam splitter, L lens, CCD charge coupled device.

After the beam splitter, the two overlapping beams are imaged on the slit plane by a photographic lens L_5. After imaging on the slit plane, the imaging object becomes one line of the sample we study. This light line passes through a beam splitter (BS_2), and after being collimated by the lens L_6 it strikes the grating, which analyses it into its spectral components. It is then back-reflected, focused by L_6 and after being reflected by the beam splitter, and is directed towards the CCD detector, through a 4-f lens system. The 4f system, formed by the lenses L_7, L_8, magnifies the image by approximately two times, in order to fill the sensor of the CCD camera.

Finally, the interference pattern is recorded by a computer connected with the camera. In Fig. 4.13 and 4.14 we show an example of the color fringes captured by a photographic camera and an experimentally detected interferogram by the black and white CCD camera, respectively. The process of analysing the retrieved spectral interferogram will be described in the next chapter.

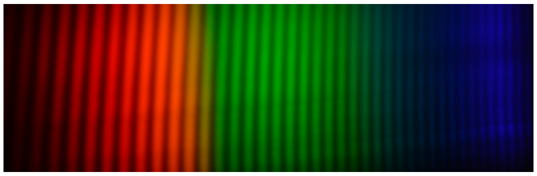

Figure 4.13: Example of a spectral interferogram as captured by a color photographic camera.

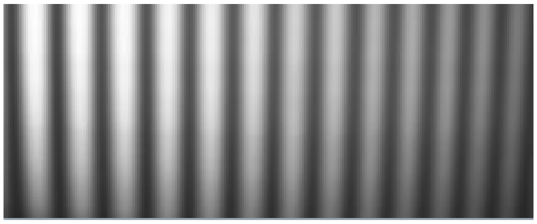

Figure 4.14: Example of a spectral interferogram as captured by the grayscale CCD camera.

Chapter 5

Experimental Procedure and Analysis of Spectral Interferograms

During the experimental procedure, the camera captures four images. First, the image of the total intensity of the interfering beams, I_{tot}. Second, after placing an obstacle in front of the sample in order to block its reflected light, we capture the intensity of the reference mirror, I_1. Third, by blocking the reference mirror's reflected light, we capture the intensity of the sample, I_2. Finally, by blocking both arms we capture the diffuse light, called "background intensity", I_b in order to be subtracted from the three previous images. This procedure is followed for all the experimental results of the present work.

5.1 Procedure of Profile Measurement

The principle idea of profile measuring is based on the OPD of the two white light beams, which are reflected from the reference mirror and the sample of interest. Using a Michelson interferometer and having replaced the mirror from the one arm with the sample under test, their interfering beam incorporates in its phase distribution the information of the sample's profile.

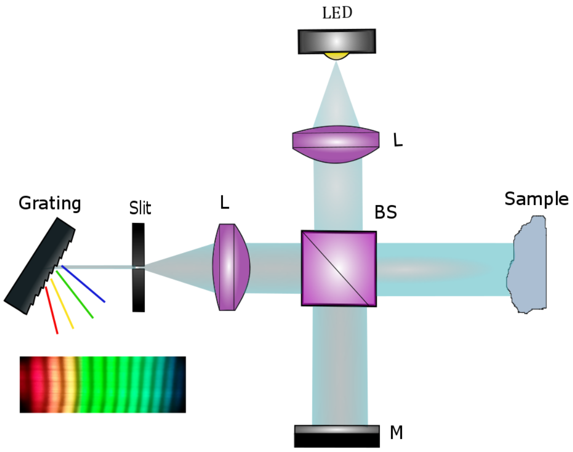

Figure 5.1: Simplified schematic representation of our device

At this point, allow us to give a short description, this time, about the beam propagation of the setup as an introduction to the profile measurement procedure. Fig. 5.1 shows a simplified schematic representation of our profilometer device, consisting only of the major parts needed for our description.The reflected reference and sample beams are imaged on the slit plane. The part of the beam which transmits through the slit, is collimated and then illuminates a grating which analyzes the light beam to its spectral components and finally is recorded from the CCD camera. Due to the presence of the slit, only a thin line of the sample surface is imaged on the CCD camera, creating a 2D image on the CCD plane since each point of this line is analyzed to its spectral components.

All lines from all points of the slit, create a 2D image which is detected by the CCD camera. In Fig.5.2 a typical 2D spcectral interferogram is shown.

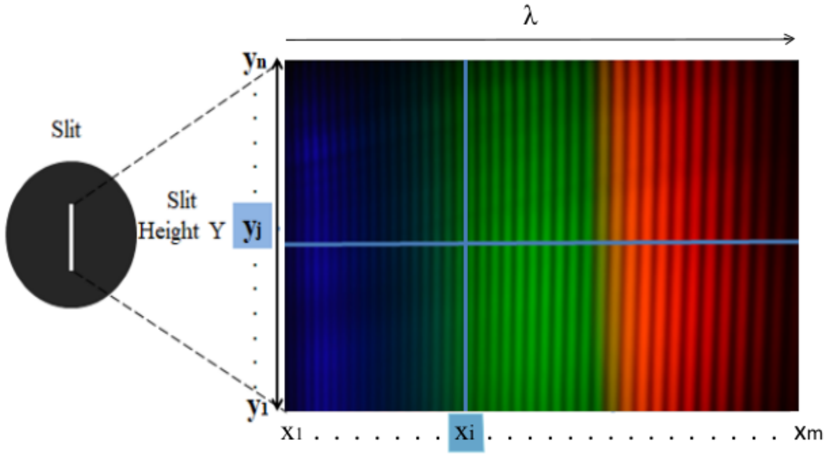

Figure 5.2: Typical spectral interferogram. Color interference fringes are clearly visible : under analysis 2D image.
Each line y_i corresponds to the spectrum of a single point on the slit, after the beam spectral interference. Each column corresponds to the image of the slit at a specific pixel and thus at a specific wavelength λ_i.

The vertical axis of the 2D image corresponds to the points on the sample that lie on a line that is imaged on the slit, while the horizontal axis corresponds to the wavelength λ. Each point of the 2D image i.e. each pixel, is a spectral interference result of the two waves; and incorporates the information about their OPD.Thus, the intensity of each one pixel can be described as

$$\begin{aligned} I_{tot}(z_j,\lambda_i) = I_{ref}(z_j,\lambda_i) + I_{surf}(z_j,\lambda_i) \\ + 2\sqrt{I_{ref}(z_j,\lambda_i) I_{surf}(z_j,\lambda_i)} \cdot cos(\frac{2\pi}{\lambda_i}2Z_j + \Delta\phi) \end{aligned} \tag{5.1}$$

When we refer to one point of the slit, we should note that corresponds to a physical width on the sample surface that depends on the magnification of the imaging system , and on the slit's width. The width of the slit sets a lower dimension limit on the physical width of the sample's line which is finally measured. In our case, the slit is 20 μm. The thinner the slit is, the less the spectral components overlap, which results in better resolution in the wavelength axis.

More specific, the terms of Eq. 5.1 are:

I˙tot(z˙j,λ_i): the intensity value at point j of the slit, or of the sample, for wavelength value λ_i after interference occurs

I˙ref(z˙j,λ_i): the intensity value at point j of the reference mirror, for wavelength value λ_i from the reference arm

I˙surf(z˙j,λ_i): the intensity value at point j of the sample, for wavelength value λ_i from the sample's arm

$2Z_j$: the OPD at point j on the line and corresponding to twice the surface height Z_j

$\Delta\phi$: the phase difference of the two beams arises, for example by the aberrations lenses induce e.g. wavelength dispersion of the beams and more generally the unequal spatial distribution of the beams.

All the terms in Eq. 5.1 can be independently measured using the CCD camera. So, in order to evaluate the term Z at all line points, we need to solve for the cosine term.

$$cos(\frac{2\pi}{\lambda_i}2Z_j + \Delta\phi) = \frac{I_{tot}(z_j,\lambda_i) - I_{ref}(z_j,\lambda_i) - I_{surf}(z_j,\lambda_i)}{2\sqrt{I_{ref}(z_j,\lambda_i)I_{surf}(z_j,\lambda_i)}} \tag{5.2}$$

Eq. 5.2 can be written:

$$cos(k_i \cdot 2Z_j + \Delta\phi) = f(I) \tag{5.3}$$

Consequently, in order to estimate Z at each point we need to estimate the phase term. In section 5.3, there is an extensive description of this procedure. Let us note here, that the term 2Z that refers to OPD is is measured in absolute values, fact that we describe in the first appendix.

5.2 Calibration of the Setup

It is necessary to calibrate our setup before we obtain experimental measurements. We estimate the range of wavelengths (spectral bandwidth) which we use for our spectral analysis, by corresponding each column in the image of the camera to a wavelength value. For the spatial calibration, we correspond one line of the image of the camera to its corresponding spatial dimensions on the sample's plane. Let us now describe analytically these two calibration procedures.

5.2.1 Spectral Calibration

In order to spectrally calibrate our system, we use commercial interference filters whose spectra transmission we have previously measured using a spectrometer. These filters are quasi-monochromatic, with a spectral width being 40 nanometers.

Each filter is placed in front of the light source and an image captured by the camera. In Fig. 5.3, we show an example of such a measurement, for an interference filter with maximum transmissivity at 600 nm.
We use four symbolometric band filters centered at 500, 550, 600, 650 nm, and we correspond the known transmission peaks to specific columns in the image.

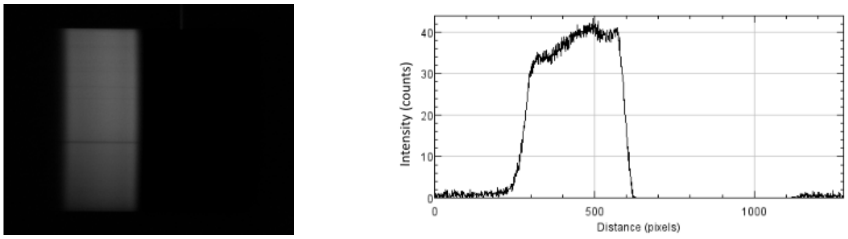

(a) (b)

Figure 5.3: Example of a spectral calibration measurement, for an interferometric band filter centered at 600 nm. (a) Image captured by the CCD, showing the filter's transmission spectra. (b) Intensity along a horizontal line in the image shown in (b).

We can then apply a linear fitting to these values, to retrieve the corresponding wavelegth for the rest of the image

$$y(nm) = \alpha \cdot x(pixel) + b \tag{5.4}$$

Having specified the parameters a and b, we can correspond each pixel of the 1280 pixels of our camera to a wavelength value. Following this approach, the total spectral bandwidth that we use for spectral analysis is found to be 475-676 nm.

5.2.2 Spatial Calibration

In order to spatially calibrate the CCD sensor, we place a needle of 580 μm width (measured by an optical microscope) in front of the sample mirror. In Fig. 5.4 we present the imaging of the needle on the slit's plane, as captured by the CCD camera.

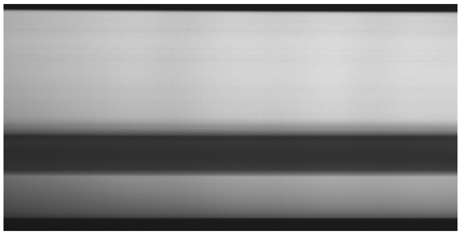

Figure 5.4: Imaging of a reference needle on the slit's plane, as captured by the CCD camera

Having measure the needle's width by an optical microscope and measuring its projection on the image, we find that 1 pixel corresponds to 3.9 μm, and the total length of the sample's line of interest is equal to 3.53 mm. Summarizing, our setup measures a line's profile of 3.53 mm length with 8 μm resolution along this line.

Profile Analysis

Three different approaching methods are followed in order to retrieve the surface profile. For all methods, the main equation we evaluate, based on metrology interference theory, can be expressed as:

$$I_{tot} = I_1 + I_2 + 2\sqrt{I_1 I_2}\cos(\frac{2\pi}{\lambda}2Z). \tag{5.5}$$

Two of these methods are automatic algorithm methods. For these algorithms, (which are later described) the input includes four intensities spectra (in 'tiff' format) and the wavelength range of the light source λ (in 'txt' format). These four intensities, which are discussed in the beginning of the present chapter, describe the total intensity of the interference pattern I_{tot}, the reference intensity I_1, the sample intensity I_2, and the background noise intensity I_b. In Fig. 5.5, we show an example of these four intensity images, with the sample of interest being a aluminum mirror.

The algorithms' output is the profile of the sample of interest.

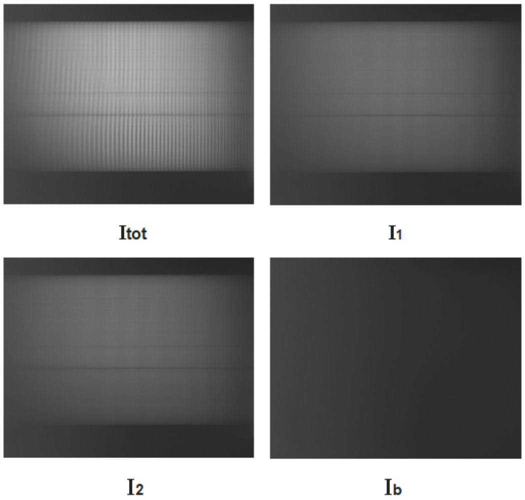

Figure 5.5: Example of the algorithm's input, for an aluminum mirror sample. The four images represent the intensities I_{tot} ,I_1 and I_2 of Eq. 5.5, as well as the background intensity I_b.

It must be noted that a horizontal line of the interference fringes (I_{tot}) corresponds to one point on the sample. An example of the intensity modulation along such a line is shown in Fig.5.6.

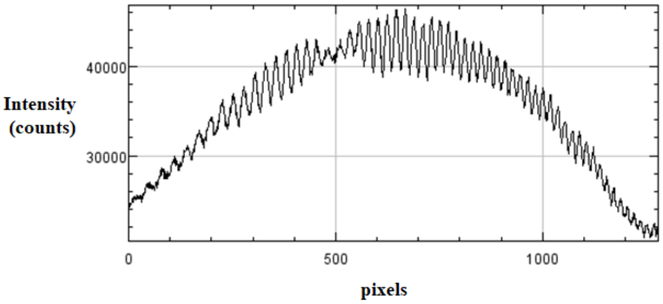

Figure 5.6: Example of the intensity modulation corresponding to one sample point.

The first step in the analysis is the spectral calibration of the system, i.e. the correlation of pixels to the wavelength, and wavelength with wavenumber k ($k = 2\pi/\lambda$). The next step, after the subtraction of noise from our signal, is plotting the cosine term of Eq. 5.5 as function of k, using:

$$\cos(\frac{2\pi}{\lambda}2Z) = \frac{I_{tot} - I_1 - I_2}{2\sqrt{I_1 I_2}}, \tag{5.6}$$

$$\cos(k \cdot 2Z) = \frac{I_{tot} - I_1 - I_2}{2\sqrt{I_1 I_2}}. \tag{5.7}$$

Subsequently, a median Gaussian filter is applied and then subtracted from the original distribution, in order to remove its envelope and detect the minimum and maximum values of the cosine term.

However, all methods are based on the evaluation of Eq.5.5. Their differentiation is only at the cosine level, see Eq. 5.7.

5.3 Profile Estimation

A straightforward approach for profile measuring is based on the equation of interference 5.5, as well as on the phase subtraction method (PSM). This straightforward approach, although very simple, can be applied in cases in which the automatic algorithms do not work efficiently, for example for cases of low contract or visibility, e.g. for samples of low reflectivity. It can also be applied as a simple validation measurement.

The method is based on visually identifying the spectral position of a discrete number of peaks (minimum 2) on the spectral interferogram and then using a simple formula to estimate the surface height. More specifically, the phase term of Eq. 5.5 reads

$$\varphi = \frac{2\pi}{\lambda}2Z \Rightarrow \varphi = k \cdot 2Z. \tag{5.8}$$

, where k is the wavenumber $2\pi/\lambda$. Thus, the phase difference as a function of the wavenumber difference Δk is:

$$\Delta\varphi = \Delta k \cdot 2Z. \tag{5.9}$$

Fig.5.7 shows a simulation of a spectral interferogram as a function of λ. Note the distribution peaks corresponding to wavelengths $\lambda_1, \lambda_2, ..., \lambda_N$.

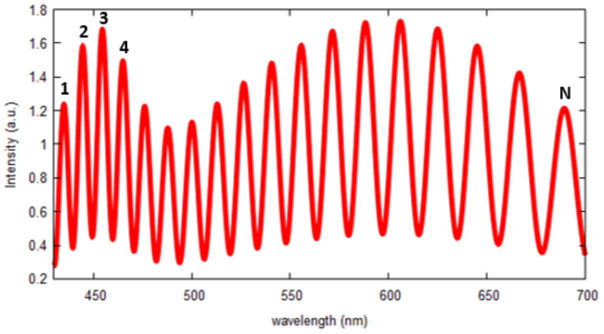

Figure 5.7: Simulation of a spectral interferogram as a function of wavelength.

For the phase difference of the two consecutive wavelengths λ_1, λ_2, we have:

$$\Delta\varphi = 2\pi = (\frac{2\pi}{\lambda_2} - \frac{2\pi}{\lambda_1}) \cdot 2Z, \tag{5.10}$$

while, for the phase difference of wavelengths λ_1, λ_3, we get:

$$\Delta\varphi = 2 \cdot 2\pi = (\frac{2\pi}{\lambda_3} - \frac{2\pi}{\lambda_1}) \cdot 2Z. \tag{5.11}$$

Similarly, the phase difference of λ_1, λ_N (where N is the number of fringes) can be expressed as

$$\Delta\varphi = (N-1) \cdot 2\pi = (\frac{2\pi}{\lambda_N} - \frac{2\pi}{\lambda_1}) \cdot 2Z. \tag{5.12}$$

Solving for Z, we can finally calculate the height as

$$Z = \frac{(N-1)(\lambda_1 \cdot \lambda_N)}{2 \cdot (\lambda_1 - \lambda_N)} \tag{5.13}$$

We shall now give an example of a manual profile measurement. The sample of interest is an aluminum step of 1.75 μm height on a Si substrate. In Fig. 5.8, we present two selected lines of interest on the 2D interference image. The upper line is chosen to be at the darker area, which corresponds to the Si substrate, while the bottom line is at the aluminum region, that is onto the step. The interferograms on the right side of Fig. 5.8 show the intensity modulation along each line. By spectrally calibrating the setup, the pixel range is correlated with wavelengths, and our spectral width is found to be 475-676 nm.

Having counted the number of fringes and estimated the values which correspond to λ_1=676 nm and $\lambda_N = 475$ nm for each line, we apply Eg. 5.13. The height Z_1 corresponding to the upper line (i.e. a point on the Si substrate) is found to be 39.37 μm. The height Z_2 corresponding to the bottom line (i.e. a point on the aluminum step) is found to be 40.96 μm. Thus, the height of the step is calculated as Z_2-Z_1=1.59 μm.

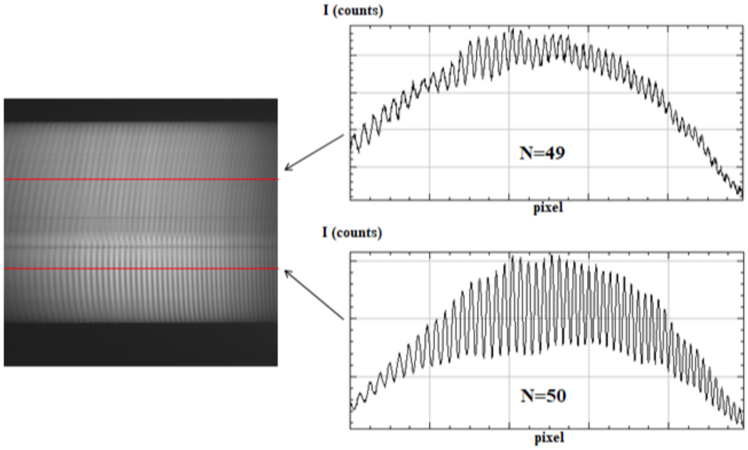

Figure 5.8: Example of the analysis for a manual profile measuring. On the left, a 2D image of the interference fringes with two selected lines of interest. On the right, two interferograms showing the intensity modulation along each line.

5.4 Profile Estimation using Phase Retrieval

Instead of using the position of the peak of a fringe we can study the evolution of the phase along the spectrum. In order to achieve automated measurements of the profile one needs to solve Eq. 5.5 that describes the intensity of the spectral interferogam, for the surface height Z. By solving the interference equation, Eg.5.5 for the cosine term we get:

$$\cos(\frac{2\pi}{\lambda}2Z) = \frac{I_{tot} - I_1 - I_2}{2\sqrt{I_1 I_2}}, \tag{5.14}$$

Solving for the phase we then get:

$$\varphi \equiv 2kZ = \cos^{-1}\left(\frac{I_{tot} - I_1 - I_2}{2\sqrt{I_1 I_2}}\right) \tag{5.15}$$

Clearly the phase φ is a linear function of the wavenumber, with a proportionality constant of $2Z$. The inverse function $\cos^{-1}$ returns a phase φ that is wrapped in the range $[0, 2\pi]$ as shown in Fig. 5.9, so phase unwrapping is necessary in order to estimate the inclination, and consequently the height.

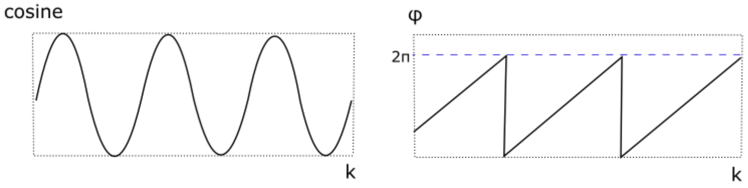

Figure 5.9: Schematic representation of a cosine $\cos(2kZ)$ and its calculated phase using $\phi = \mathrm{k}Z$

A disadvantage of this approach is that it is sensitive to the presence of noise.

In Fig. 5.10, Fig. 5.11, are shown schematic representations of wrapped and unwrapped phase as a function of wavenumber k concerning a noiseless signal and a signal with noise, respectively.

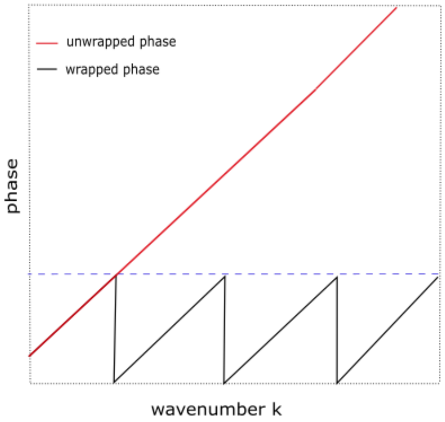

Figure 5.10: Schematic representation of phase unwrapping of a noiseless signal

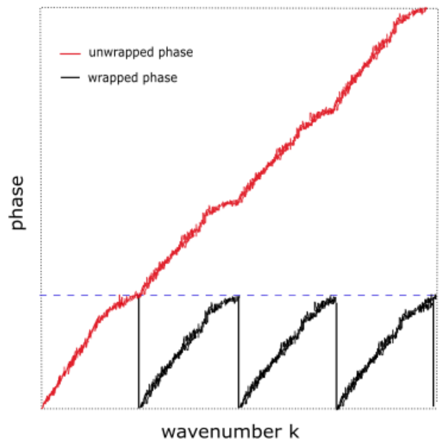

Figure 5.11: Schematic representation of phase unwrapping of a noisy signal

In this case, applying a linear fitting does not insures the precise phase value and this results in possible unreliable measurement results. Two example results are illustrated here, with the first presenting low and the second presenting high noise signal.

Examples of simulated measurement results using the Phase Retrieval Method

By making simulations of noiseless and noisy signal spectral fringes referring to a groove like step, we test the efficiency of phase retrieval method.

Simulation of noiseless and noisy signal measurement results

The measurement results of simulated noiseless and noisy spectral fringes are shown in Fig.5.12 and Fig.5.13, respectively.

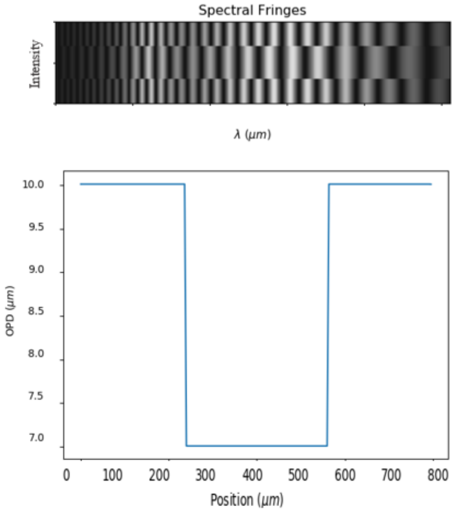

Figure 5.12: Noiseless spectral fringes and measurement result using phase retrieval method.

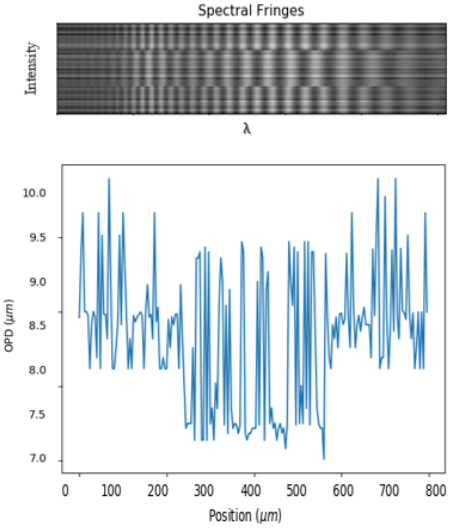

Figure 5.13: Noisy spectral fringes and measurement result using phase retrieval method

From the above figures, we can see that when noise exists in data, fact that characterize real data, the measurement results appear spikes and errors and renders the measurement unsatisfactory.

5.5 Optimized Profile Analysis

Here we present a more sophisticated approach to recover the spatial frequency term in the phase φ in Eq. 5.7. This approach is based on directly estimating the spatial frequency in the term $\cos(2Zk)$ avoiding the double step of firstly recovering the phase and then, from the inclination of the curve $\varphi(k)$ the height Z. The algorithm of profile measuring we use for analyzing our data is developed by Vangelis Tzardis, diploma thesis, 2019. In this approach we directly apply a Fourier Transform (FT) to our noisy data and from the peak in the FT space we determine the dominant spatial frequency of our signal.

Since our signal is not an ideal cosine, i.e. it incorporates a range of spatial frequencies, a Fourier transform is applied and the carrier frequency of the signal arises. In the following Fig. 5.14, Fig.5.15, Fig.5.16, are shown examples of our signal, a Fourier transform of this signal and the retrieving method of the carrier frequency, respectively.

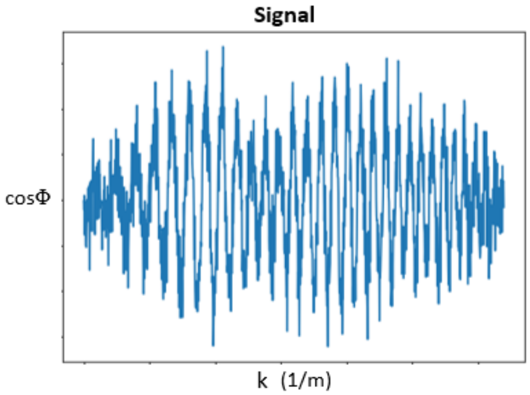

Figure 5.14: Example of the signal of a sample. The signal is not an ideal cosine.

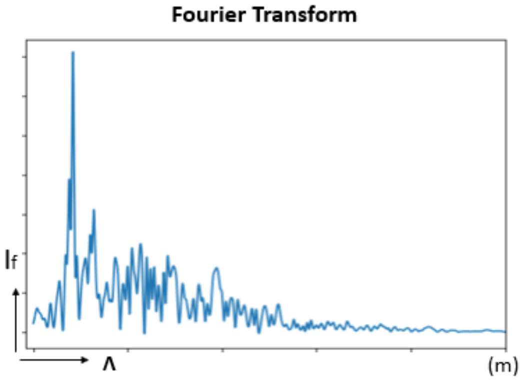

Figure 5.15: Fourier transform of the signal.

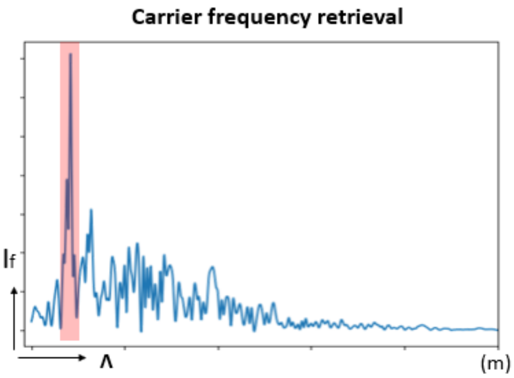

Figure 5.16: A Gaussian filter applied on the signal Fourier transform in order to retrieve the carrier frequency.

From this carrier spatial frequency, we can estimate the surface height Z by:

$$Z = \pi f. \tag{5.16}$$

Comparison of Fourier transform and Phase retrieval methods

We compare Fourier transform and Phase retrieval methods by utilizing both in simulated noisy signal. The results are shown in Fig.5.17

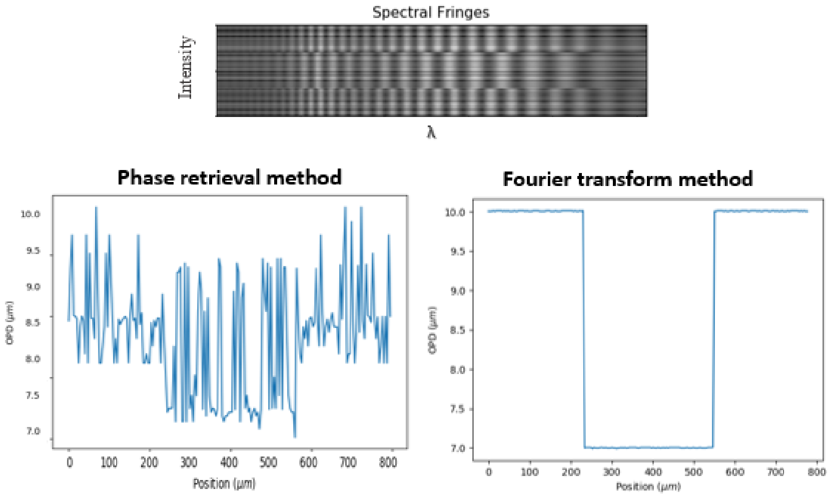

Figure 5.17: Measurement results of phase retrieval and Fourier transform methods.

In the above figure, the simulated noisy spectral fringes refer to a groove like sample, same used in previous paragraph and both methods results are presented. It is obvious, that Fourier transform method appears to be robust in noise.

Chapter 6

Experimental Results

Our general methodology is the following:

- First, we provide a validation for the performance of our device. More specifically, we measure five surface profiles which had been previously measured independently by using reliable and established techniques and setups. These independent measurements can then be used as reference, allowing us to evaluate the efficiency of our setup, and characterize its accuracy.
- Having managed to validate our device, we shall proceed in measuring and characterizing the surface topography of unknown samples of interest.

6.1 Sample I: Flat Aluminum Mirror

First, we must characterize the resolution and the possible measurement errors of our setup. In order to do this, we use a flat mirror of 2.5 μm flatness and a $\lambda/10$ surface quality.

The OPD between the two mirrors (reference and sample) is represented in Fig. 6.2.

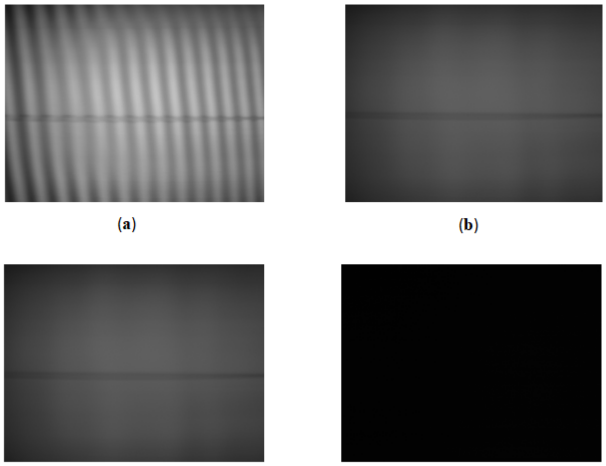

(a) (b)

(c) (d)

Figure 6.1: Images for the mirror sample profile measurement. (a) Total intensity of both mirrors. (b) Intensity of reference mirror. (c) Intensity of sample mirror. (d) Background intensity.

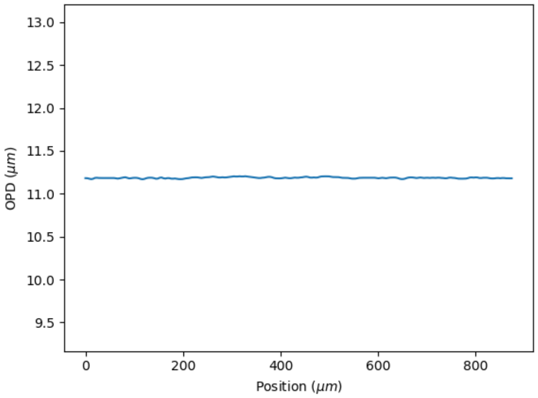

Figure 6.2: OPD between the surfaces of the two mirrors.

In fact, the profile of the mirror sample is the difference between the roughness of the two mirrors. This roughness difference also characterizes the minimum error in our profile measurements. Zooming in Fig. 6.2, we can see the roughness in detail as shown in Fig. 6.3.

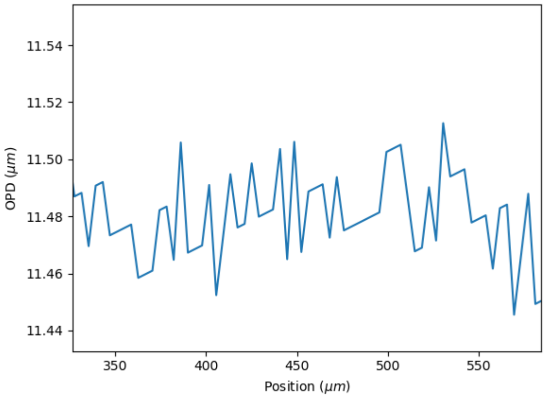

Figure 6.3: Roughness of mirror's profile

By calculating the standard deviation of the surface roughness, we find it to be equal to 10 nanometers, and we consider this value is our device precision.

The specifications of the two mirrors used as sample and reference indicate that they both should exhibit a surface quality of $\lambda/10$. From Fig. 6.3, we can see that the surface height variation is 20 nm (peak-peak) a value which is close to the 50 nm that corresponds to the $\lambda/10$ flatness quality. This translates to a surface profile roughness of 50 nm. Taking into account that the subtraction of two distributions has a lower standard deviation by a factor of $\sqrt{2}$ we then get that we should expect a variation of 35 nm, very close to the measured value.

6.2 Sample II: A Sample of Stylus Profilometer

We measure a sample of the Stylus profilometer sample, shown in Fig.6.4. This sample consists of a flat, thick piece of glass with two, rectangular in shape, grooves of well defined depth engraved on it's surface. The depth of these grooves have been also measured using A-step technique, a contact profilometry technique and according to that the grooves depth results are 9.3 and 9.5 μm, respectively.

Figure 6.4: Sample II: Stylus profilometer sample

Each groove causes a change in the fringes modulation as may be seen in Figs.6.5 and 6.6.

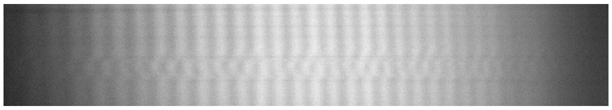

Figure 6.5: Spectral fringes from the 9.3 μm nominal value of Stylus profilometer's groove depth.

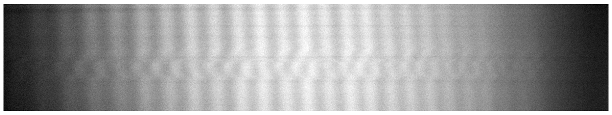

Figure 6.6: Spectral fringes from the 9.5 μm nominal value of Stylus profilometer's groove depth.

The profiles of 9.6 μm and 9.7 μm Stylus sample grooves are measured as shown in Figs.6.2 and 6.8 respectively.

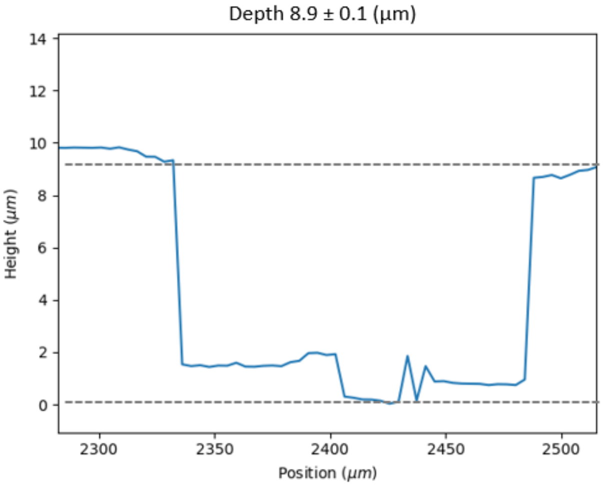

Figure 6.7: P
rofile of 9.3 μm nominal value of Stylus profilometer's groove depth.

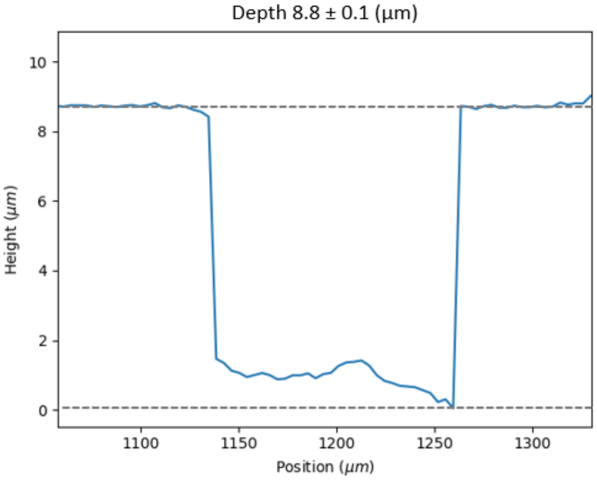

Figure 6.8: Profile of 9.5 μm nominal value of Stylus profilometer's groove depth.

As we can see, the measured values of the grooves' height are respectively, 8.9±0.1 μm and 8.8 ±0.1 μm, where, error is the sum of the standard deviations of the depth's top-line and baseline..

The discrepancy between these results is possibly due to soft surface deposits, like dirt, in the bottom of the sample grooves. In contrast to a contact profilometer which "cleans out" such soft over layers as it scan though a hard surface, our optical profilometer measures the actual surface topology.

If we examine the sample's image from an optical microscope, see Fig.6.9, we can see some of these defectst.

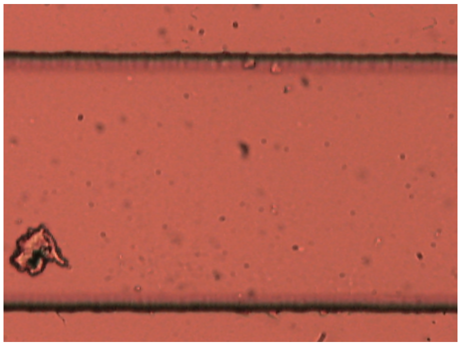

Figure 6.9: Stylus profilometer's groove image from optical microscope.

6.3 Sample III: Aluminum film of 500 nm sputtered on a flat Al substrate forming a step

The third sample we measure is a 500 nanometers of height Aluminum Step on Aluminum substrate which is fabricated by using the magnetron sputtering technique. A typical image of the spectral interference fringes is shown in Fig. 6.10.

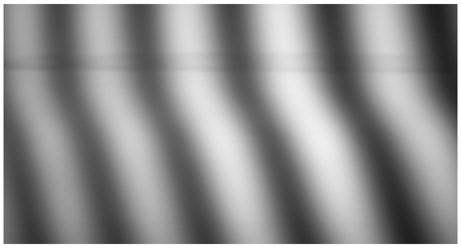

Figure 6.10: Spectral fringes modulation of 500 nm step.

The experimental result of the profile is 480±50 nm and it is shown in Fig.6.11.

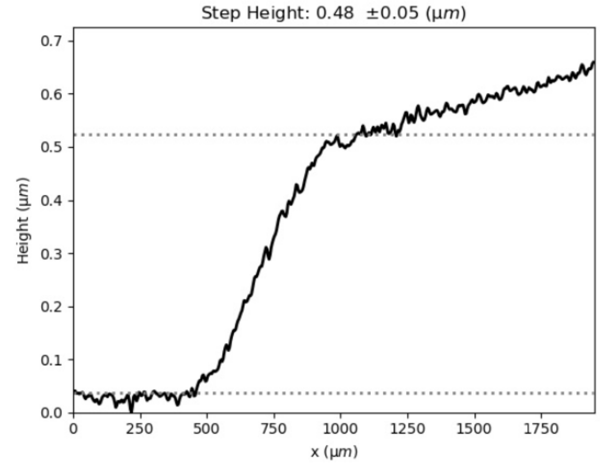

Figure 6.11: Profile of 500 nm Aluminum step.

The % error equals to 4% and the deviation error (de) equals to 0.4 σ. where de is given by

$$de = \frac{|H_t - H_e|}{error} \tag{6.1}$$

6.4 Sample IV: Aluminum Step on Si Substrate

The fourth sample we measure is an Aluminum Step on Si substrate, Fig.6.12 of 1.75 μm height, which is also created by using the magnetron sputtering technique.

Figure 6.12: Sample IV: 1.75 μm Aluminum step on Si substrate.

The spectral fringes modulation and the measured profile of this sample are shown in Fig.6.13 and Fig.6.14 respectively.

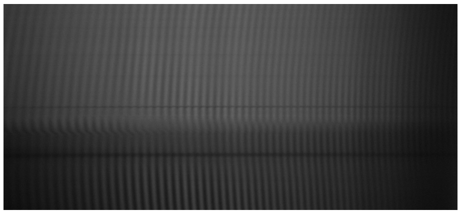

Figure 6.13: Sample IV: Spectral fringes modulation from the 1.75 μm Aluminum step nominal height.

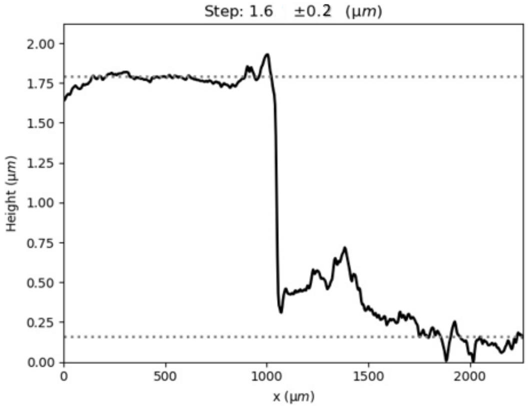

Figure 6.14: Measured profile of the Aluminum Aluminum step on Si substrate.

As we can see in Fig.6.14, the measurement is 1.6±0.2 μm and comparing it with the nominal value: 1.75 μm, we find the deviation error to be equal to 0.75 and agreement on the results.

6.5 Sample V: Spin Coated Polymer on Glass

The polymer sample is developed by material development synthesis technique and coated onto a thin glass by spin coating.A step was fabricated to allow the sample thickness to be measured. An additional measurent of A-step profilometer which is a contact profilometer took place, and the nominal thickness value of the sample is 6.1 μm. In Fig. 6.15, Fig. 6.16 and Fig. 6.17 are shown the polymer sample, spectral fringes and the measured profile respectively.

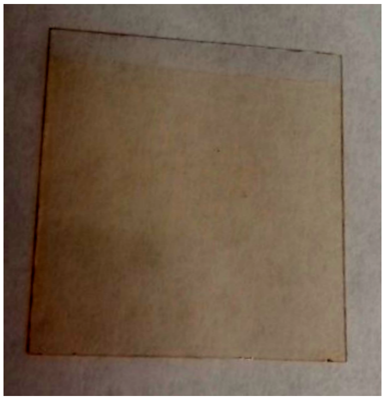

Figure 6.15: Image of the polymer sample.

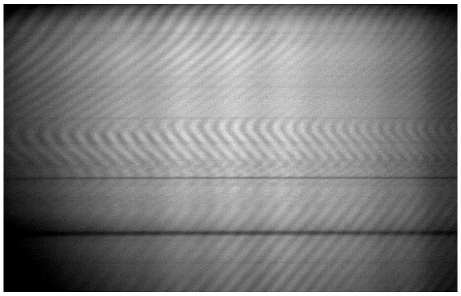

Figure 6.16: Interference fringes distribution from polymer coating sample.

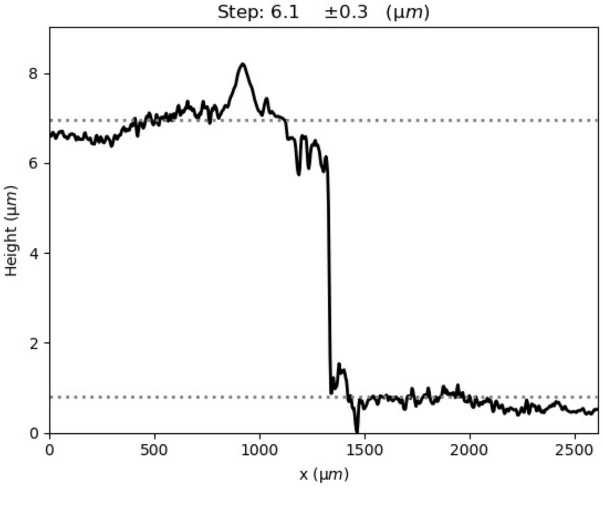

Figure 6.17: Profile of the polymer coating onto the glass.

As we can see in Fig. 6.17, the polymer thickness found to be equal to 6.1±0.3 μm. The experimental error is calculated as the sum of the standard deviations of the step's top-line and baseline. Our experimental measurement in comparison with the A-step profilometer measurement totally agree.

6.6 Polymer Coating onto thin glass

Several polymer samples developed by the same described technique, have been measured in order to estimate their thickness and their surface smoothness. Allow us to demonstrate this measurement results in a shorter form, by presenting some of them in figures and by marking all results in a table.

In Fig. 6.18, are presented the profile measurement results. The term step refers to the polymer's thickness since the upper profile is the polymer's profile and the bottom is the profile of the glass and thus the profile of the whole structure can be seen as a profile of a step. In this figure we present an overview of the thickness measure results.

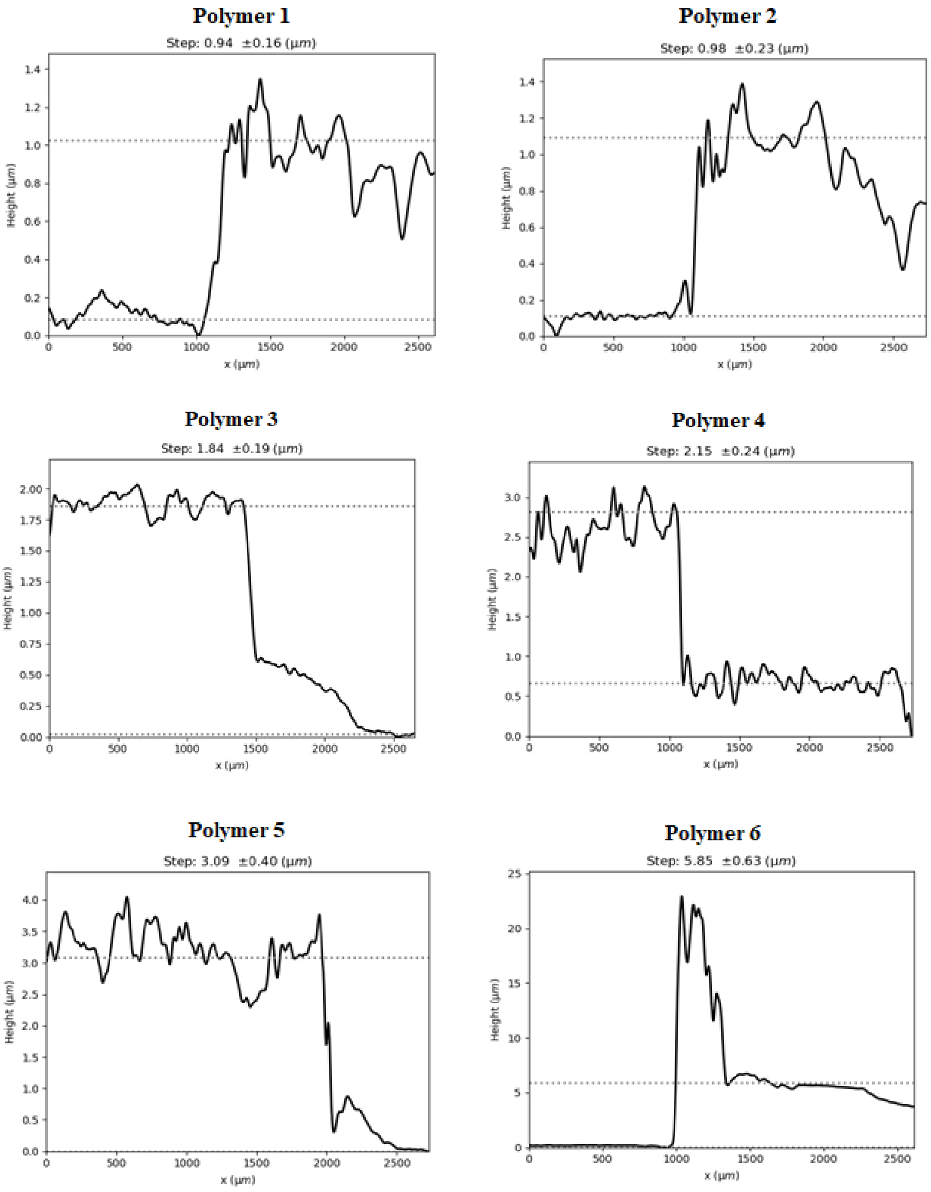

Figure 6.18: Polymers' profile and thickness results.

These samples were also measured by a different profilometry setup, which is based on WLSI technique and measures two-dimensional. The result of polymer 5 surface can be seen in Fig. 6.19.

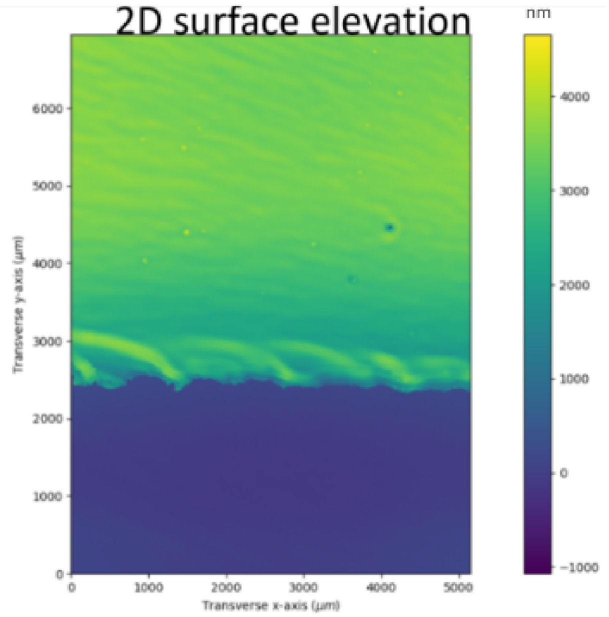

Figure 6.19: 2D profile of sample polymer 5 measured by the WLSI technique. The colorbar shows the height values along the z axis (V.Tzardis, 2019).

Our method measures along a vertical line on the sample surface.
The following table contains a summary of all polymer thickness results which have been measured. Moreover, isolating the polymer's area, we characterize its surface roughness.

Table 6.1: Polymer Measurement Results.

Polymers	Thickness (μm)	Error (μm)	Roughness (μm)
Polymer 1	0.94	0.27	0.13
Polymer 2	0.98	0.38	0.12
Polymer 3	1.84	0.19	0.08
Polymer 4	2.15	0.4	0.32
Polymer 5	3.09	0.23	0.35
Polymer 6	5.85	0.39	0.34
Polymer 7	0.72	0.1	0.05
Polymer 8	1.25	0.64	0.11
Polymer 9	1.39	0.2	0.1
Polymer 10	0.93	0.18	0.06
Polymer 11	6.13	0.48	0.14
Polymer 12	5.22	0.35	0.16
Polymer 13	3.49	0.09	0.28

In the following figures, Fig. 6.20 and Fig. 6.21 we can see the roughness of polymer 4 and polymer 5 (shown in Fig.6.18). The following roughness figures are calculated by applying a median Gaussian filter on the surface profiles data, and then subtracting it from the initial profile data. The rms value reads Eq. **??**.

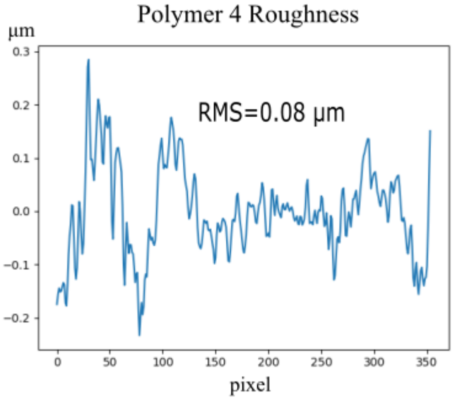

Figure 6.20: Roughness and roughness rms of polymer 4. The rms value is equal to 0.08μm

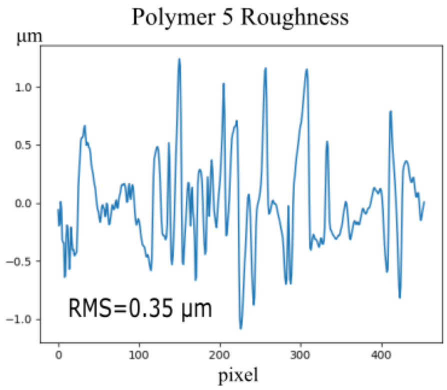

Figure 6.21: Roughness and roughness rms of polymer 5. The rms value is equal to 0.35 μm.

These polymer profiles are further analyzed using four metrics which characterize their topography. They are namely, RMS: root mean square height, R_{max}:maximum peak to valley height, Rku: kurtosis of the roughness profile. These metrics are defined and discussed in Appendix B. The results of the application of the metrics on the polymer surface profiles are presented in Table 6.2. The polymers here are in the same order as in Table 6.1.

Table 6.2: Metric results in polymer surface measurements.

Polymers	M (μm)	RMS (μm)	R˙max (μm)	Rku
Polymer 1	1	0.172	0.402	2.98
Polymer 2	1	0.227	0.434	2.799
Polymer 3	2	0.075	0.147	2.69
Polymer 4	2	0.08	0.516	2.65
Polymer 5	3	0.350	0.847	3.235
Polymer 6	6	0.792	1.355	2.59
Polymer 7	1	0.38	0.601	1.94
Polymer 8	1	0.109	0.196	2.208
Polymer 9	1	0.215	0.36	1.74
Polymer 10	1	0.031	0.072	4.119
Polymer 11	6	0.792	1.355	2.59
Polymer 12	5	0.824	1.124	2.83
Polymer 13	3	0.362	0.764	2.05

From the presented results, we conclude that the polymer surfaces have a rather smooth variation in height distribution along the line, and most of them do not exhibit spikes at all (Rku<3). The surfaces can be characterized as bumpy, wavy.

Chapter 7

Measurments performed at High Repetition Rates

Measurement of Profile Changes over Time

In this chapter, we demonstrate profile measurements of a surface that changes over time. We show that spectral interferometry is an ideal technique for performing rapid, high-resolution measurements, with no restrictions in the surface hardness. The time resolution is limited only by the rate at which the camera can capture images. which, in our case, it is up to 170 frames per second and is translated to 6 msec of time resolution.

The experiment that takes place in this chapter concerns the study of the decay rate of a varnish layer which is been applied on a thin piece of glass. In Fig. 7.1, shows a cartoon of the varnish layer on the glass and the captured image of the corresponding spectral fringes.

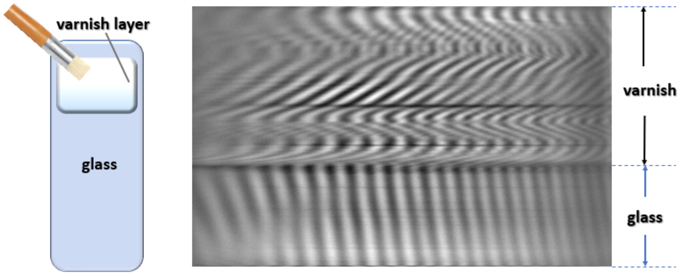

Figure 7.1: Cartoon of varnish layer on thin glass and its corresponding experimental spectral fringes.

Having as a sample the varnish layer on a thin glass and as a reference an aluminum mirror, we record a video with frame rate of 170 frames per second and 8.42 sec duration. We captured 1434 frames at 6 msec/frame.

In the following figures: Fig. 7.2, Fig. 7.3 are shown the spectral fringes and the height measurement results for three time instances.

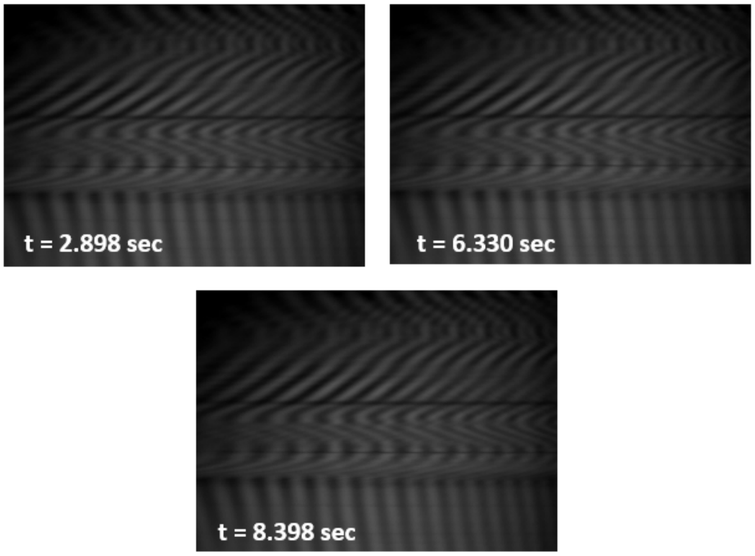

Figure 7.2: Varnish spectral fringes for three time instances. At the varnish area, can be observed small changes in fringes periodicity.

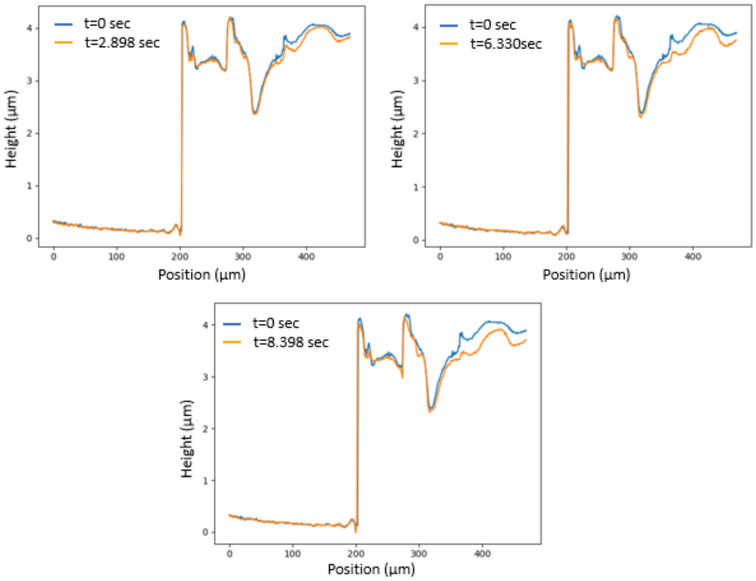

Figure 7.3: Varnish height results for three time instances.

In Fig. 7.3 we can see the height of the varnish layer applied on the glass at four different time intervals. The blue curve in all graphics, corresponds to height result at time zero, in other words it corresponds to the first measurement. The orange curves refer to height results for time instances: 2.898 sec, 6.330 sec and 8.398 sec. On their left side, the linear area corresponds to the glass surface while the wavy area refers to the varnish. Let us note here that the glass surface used as a reference, thus appears to be equal to zero in height. We can clearly see that height decreases in the course of time. In the following figure, are plotted in one graphic the height results, corresponded to the same time instances.

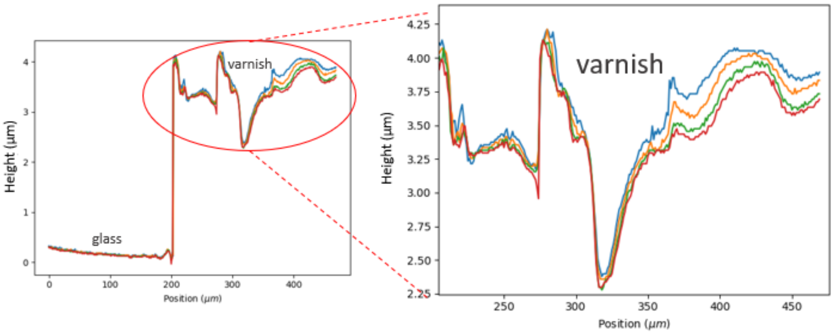

Figure 7.4: Varnish height results for five time instances.

In fig. 7.4, the blue curve corresponds to the first measurement t=0 sec, the orange curve corresponds to 2.898 secc, the green curve, to t=6.330 sec and the red, to 8.398 sec. We can see much more clearly here, that varnish height decreases along time, a fact which was of course anticipated since the varnish solvent evaporates along time.

By analyzing the total number of frames captured during the whole process time duration 8.42 sec, we can monitor this surface evaporation though the resulting film height or thickness change as a function of time, as shown in Fig. 7.6.

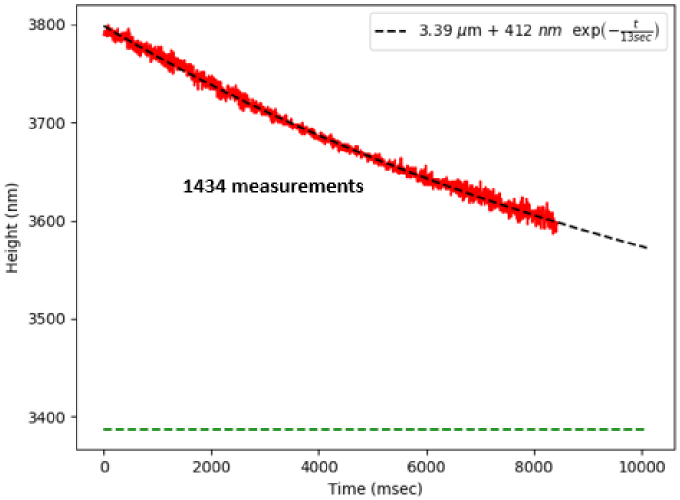

Figure 7.5: Height or thickness of the varnish coating on glass as a function time.

Vertical axis is the varnish height and horizontal axis is time in msec. The total number of measurements is 1434 while the time resolution is 6 msec. By applying a fitting we see that this solvent evaporation driven shrinking is well described by an exponential law with a time constant of 13 sec. In the end of this process($t \to \infty$), the varnish coating will reach 3.39 microns.

The rate of varnish decay is also estimated and it is shown in Fig. 7.6.

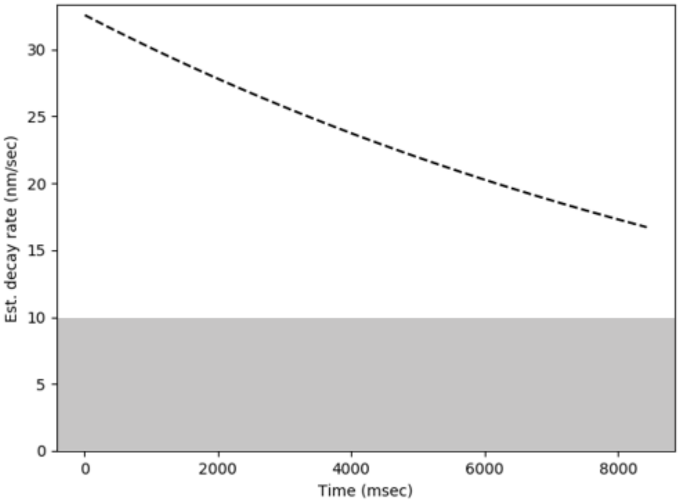

Figure 7.6: Decay rate of varnish.

As we can see in the above figure (using the exponential fit of Fig. 7.6), the decay rate varies from 30 nm/s down to 18 nm/s. Theoretically our device can not measure can measure changes in thickness or surface height as at rates lower than 10 nm/s per sec since this number corresponds to our resolution (see gray area in Fig. 7.6).

Conclusions and Future Work

The profilometer implemented in the laboratory in combination with an automated measurement and profile analysis software developed in Python, can successfully measure the height profile of a line on the surface of a sample, without any scanning. The accuracy and ability to measure depends on the reflectivity of the sample. In the best case of a high reflectivity sample (e.g. a mirror), the precision of the method is in the order of 10 nm. The range in which we can measure successfully is up to 100 μm.

Improvements

Portability

One of the future plans is making our setup more compact and easily portable. In fact, this is feasible even at the present device, but improvements need to be done.

The basic change needed to be done done is the spatial confinement of the setup regarding all of its three dimensions, length, width and height, prioritizing the height. Decreasing the height of the optical parts, the stability of the device is improved, since we achieve to reduce the vibration noise. For this purpose, we created designed drawings of the mechanical components e.g. holders, posts, mounts, by using FreeCad, an open source CAD software. They are designed in suitable dimensions in order to fit to a more compact setup. Some examples of the re-designed compact components are shown in Fig.7.7.

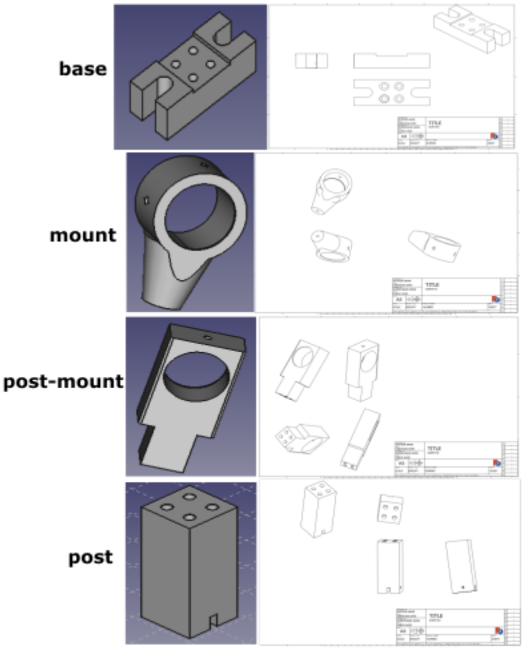

Figure 7.7: Drawings of the mechanical components using the Freecad software.

Placement of the Sample

In the present version of the profilometer the sample is placed vertically. This can create difficulties when time depended measurements take place, especially when the sample under test is fluid since gravity affects the results. A solution would be the use of two optical elements (in both arms for preserving the interference principles) which would to place the sample horizontally.

Transverse Resolution

Another important improvement that could be made is the enhancement of the transverse spatial resolution. The poor spatial resolution leads to averaging over a finite area of the sample that will eventually blur the height profile. The resolution in x-axis could improved by using a higher magnification imaging optical system.

Appendices

Appendix A

Absolute OPD Measurements

The device measures the absolute optical path difference between the sample and the reference mirror. The periodicity of the spectral fringes is the key of profile measurement. Having as a reference point the OPD be equal to zero (OPD=0,) there is no way to distinguish if the sample is further or closer from the reference mirror. The fringes density is exactly the same for symmetric distances of the zero OPD point. This, can be explained by observing Fig. A.1

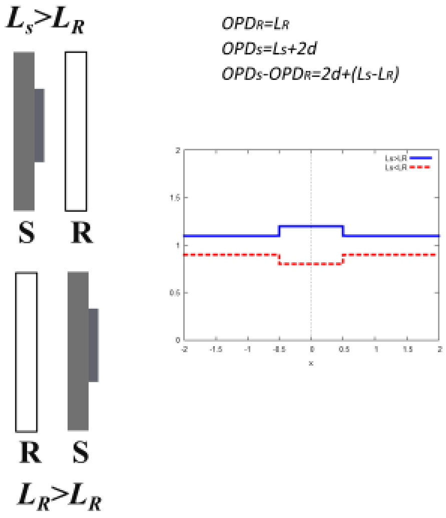

Figure A.1: Absolute OPD measure

As we can see in Fig. A.1, the OPD value is never negative or positive. The measured OPD refers always to the absolute value of OPD. Here, are represented the OPD results and the corresponding spectral fringes of a reflecting step in cases where $L_s > L_R$ and $L_s < L_R$, respectively, where L_s refers to the optical length of the sample and L_R refers to the optical length of reference mirror. We observe here, that a sample as that with a step on it, can be measured either as a sample with a step, either as a sample with a groove, depending on the configuration of the interferometer.

In the following figures, are represented the spectral fringes and the corresponding OPD results of simulated data. The first pair of figures correspond to 10 μm "positive" displacement of the sample from the reference i.e. $L_s - L_R$ =10 μm ($L_s > L_R$), and the second example corresponds to a "negative" displacement of the sample from the reference mirror i.e. $L_s - L_R$ =-10 μm ($L_s < L_R$)

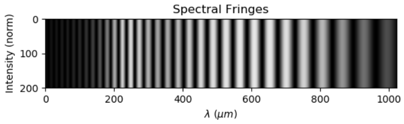

Figure A.2: Spectral fringes in case where $L_s - L_R$ =10 μm.

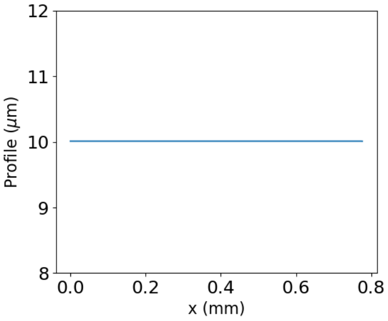

Figure A.3: OPD result in case where $L_s - L_R$ =10 μm.

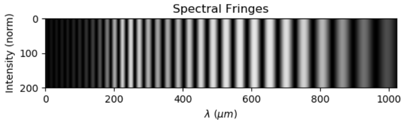

Figure A.4: Spectral fringes in case where $L_s - L_R$ =-10 μm.

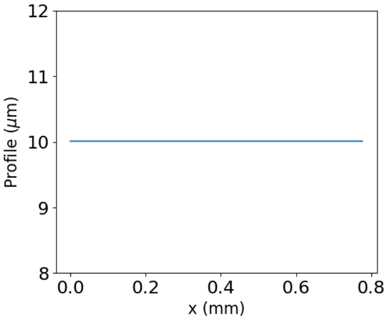

Figure A.5: OPD result in case where $L_s - L_R$ =-10 μm.

As we can see in both cases, the OPD results are same, positive and equal to 10 μm.

In both cases the measurement result is correct, but we have to translate OPD to topology based on the configuration of the interferometer we use.

Appendix B

Algorithm of Profile Measuring

```
import matplotlib.pyplot as plt
import numpy as np
from matplotlib.figure import Figure

    try:
import tkFileDialog
except:
import tkinter.filedialog as tkFileDialog

    try:
import Tkinter
except:
import tkinter as Tkinter

    import imageio as io
import glob
from gatspy.periodic import LombScargleFast
from scipy.interpolate import interp1d
from scipy.ndimage import gaussian_filter,
gaussian_filter1d
from scipy.optimize import curve_fit
from scipy.signal import fftconvolve
import time
from numpy import std

    def func(x, a, b):
return a * x + b
”””
```

```
change ROI
”””
ROI=[100,800,0,1280]

    um=1e-6

    root = Tkinter.Tk()
root.wm_attributes(’-topmost’, 1)
root.withdraw()

    ResultDir =
tkFileDialog.askdirectory(parent=root,title=’Pick the folder that contains the
interferometer images’)
FileList1=glob.glob(ResultDir+’
’+’*Is_*’+’.txt’)
FileList2=glob.glob(ResultDir+’
’+’*Is_*’+’.tiff’)
FileList3=glob.glob(ResultDir+’
’+’*Is_*’+’.tif’)

    if len([FileList1, FileList2]) == 0:
raise Exception(”No interferometer files were found”)

    load files
if FileList1:
Itot = np.loadtxt(ResultDir+’
’+’Is_tot.txt’)
Ir = np.loadtxt(ResultDir+’
’+’Is_r’+’.txt’)
Ib = np.loadtxt(ResultDir+’
’+’Is_b’+’.txt’)
elif FileList2:
Itot = io.imread(ResultDir+’
’+’Is_tot’+’.tiff’)[ROI[0]:ROI[1],ROI[2]:ROI[3]]
Is = io.imread(ResultDir+’
’+’Is_s’+’.tiff’)[ROI[0]:ROI[1],ROI[2]:ROI[3]]
Ir = io.imread(ResultDir+’
’+’Is_r’+’.tiff’)[ROI[0]:ROI[1],ROI[2]:ROI[3]]
Ib = io.imread(ResultDir+’
’+’Is_b’+’.tiff’)[ROI[0]:ROI[1],ROI[2]:ROI[3]]
Itot = Itot.astype(float)
Is = Is.astype(float)
Ir = Ir.astype(float)
Ib = Ib.astype(float)
Itot = io.imread(ResultDir+’
’+’Is_tot’+’.tif’)[ROI[0]:ROI[1],ROI[2]:ROI[3]]
```

```
Is = io.imread(ResultDir+’
’+’Is_s’+’.tif’)[ROI[0]:ROI[1],ROI[2]:ROI[3]]
Ir = io.imread(ResultDir+’
’+’Is_r’+’.tif’)[ROI[0]:ROI[1],ROI[2]:ROI[3]]
Ib = io.imread(ResultDir+’
’+’Is_b’+’.tif’)[ROI[0]:ROI[1],ROI[2]:ROI[3]]
Itot = Itot.astype(float)
Is = Is.astype(float)
Ir = Ir.astype(float)
Ib = Ib.astype(float)

    lamda = np.loadtxt(ResultDir+’
’+’lamda.txt’) lamda = lamda[ROI[2]:ROI[3]]

    s = np.shape(Itot)
rows = s[0]
cols = s[1]

    t = time.time()

    k = 2*np.pi/lamda
    if cols
Itot = Itot[:,:-1]
Is = Is[:,:-1]
Ir = Ir[:,:-1]
Ib = Ib[:,:-1]
k = k[:-1]
cols -= 1

    Is_g = gaussian˙filter1d(Is, sigma=3, axis=1)
Ir_g = gaussian˙filter1d(Ir, sigma=3, axis=1)
Ib_g = gaussian˙filter1d(Ib, sigma=3, axis=1)
corrected measured modulation
eps = np.finfo(np.float64).eps
nom = 2.0*np.sqrt(Is_g)*np.sqrt(Ir_g)
nom[np.where(nom==0)] = eps
Ipr = (Itot-Is_g-Ir_g-Ib_g)/nom
Ipr = Itot
    EXTRA PRE-PROCESSING
Ipr_g = gaussian_filter1d(Ipr, sigma=11, axis=1)
Ipr_mod = Ipr - Ipr_g
Ipr_modg = gaussian˙filter1d(Ipr_mod, sigma=3, axis=1)
Iprmodg2 = Ipr_modg - np.median(Ipr_modg)

    ANALYSIS
```

```
    num_resample = cols
k_new = np.linspace(k[0], k[-1], num_resample)
dk = abs(k_new[0] - k_new[1])
Fn = 1/(2*dk)
Nfreqs˙f = num_resample
f_axis = np.linspace(0, Fn, Nfreqs_f//2+1)
z = np.zeros(rows)

    for i in range(rows):
f_rsmpl = interp1d(k, Iprmodg2[i], kind=’cubic’)
Ipr_new = f_rsmpl(k_new)

    fourier = np.fft.fft(Ipr_new, n=Nfreqs_f)
fourier = np.abs(fourier)
fourier = np.fft.fftshift(fourier)
fourier = fourier[Nfreqs_f//2:]

    Nf_times = 20
f_axisnew = np.linspace(f_axis[0], f_axis[-1], Nfreqs_f*Nf_times)
f_rsmpl2 = interp1d(f_axis, fourier, kind=’cubic’)
fourier_new = f_rsmpl2(f_axisnew)

    ____________________________________________________ ”””
trim ’sigma_f’ for better result
”””
sigma_f = Nf_times*1
Nf_times/4
fourier_g = gaussian_filter(fourier_new, sigma=sigma_f)
argmax_idx = np.argmax(fourier_g)
z[i] = np.pi*f_axisnew[argmax_idx]/um

    if i == rows//2:
plt.figure()
plt.title(’sigma_f = abs( FWHM(fourier_curve)/2 )’)
plt.plot(fourier_new)
plt.plot(fourier_g)

    plt.figure()
plt.plot(fourier_new)
____________________________________________________

    Xscale = 3.9
dx = Xscale*np.arange(rows)
popt, pcov = curve_fit(func, dx[:], z[:])
stepProfile = z - popt[0]*dx
plt.figure()
plt.title(’Profile’)
```

```
plt.ylabel('Height (μm)')
plt.xlabel('Position (μm)')
plt.get_current_fig_manager().window.raise_()
plt.plot(dx,z)
plt.savefig(ResultDir+'
'+'Profile')

    plt.figure()
plt.title('S_Profile')
plt.ylabel('Height (μm)')
plt.xlabel('Position (m)')
plt.get_current_fig_manager().window.raise_()
plt.plot(dx,stepProfile)
plt.savefig(ResultDir+'
'+'S_Profile')
np.savetxt(ResultDir+'
'+'S_Profile, stepProfile)

    elapsed = time.time() - t
print('Fourier  Fast Lombscargle:
z_mean = np.mean(z)
print("z_mean",z˙mean)
np.savetxt(ResultDir+'
'+'Profile.txt', z)
np.savetxt(ResultDir+'
'+'dx.txt', dx)
np.savetxt(ResultDir+'
'+'S_Profile.txt', stepProfile)

    z_rms = np.sqrt(np.mean((Step_g*1000)**2))
dict = 'rms' :z_rms , 'std' :std(Step_g*1000)
std = sqrt(mean(abs(x - x.mean())**2)) a measure of the spread of a distribu-
tion f = open(ResultDir+"
rms_std.txt","w")
f.write( str(dict) )
f.close()
```

Appendix C

Metric Definition for Surface Topography Characterization

C.1 Mean (M)

Mean is the arithmetic average of a set of values. It is calculated by summing the data and dividing by the number of points, see Eq.C.1. The Mean describes the central location of the data.

$$\overline{z} = \frac{1}{n}\sum_{i=1}^{n} z_i \tag{C.1}$$

C.2 Root Mean Square (RMS)

RMS is the root mean square deviation line from the center line. The center line is defined as the best fit surface selected with the remove function. It is given from Eq.**??**

C.3 Maximum Peak to Valley Height (R_{max})

The maximum peak to valley height R_{max} describes the greatest peak to valley distance within any one sample length, (Fig. C.1)

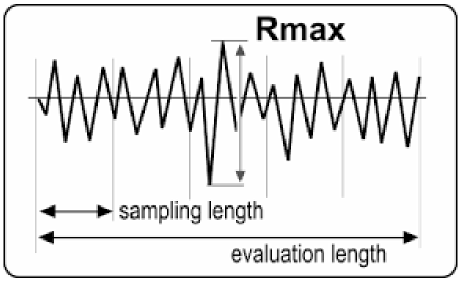

Figure C.1: Definition of R_{max} metric.

C.4 Kurtosis of the roughness profile (Rku)

Rku is a measure of the randomness of heights, and of the sharpness of a surface. A perfectly random surface has a Rku value of 3. The further the result is from 3, the less random and more repetitive the surface is. Surfaces with spikes have higher Rku values, while bumpy surfaces have lower (Fig. **??**). The definition of Rku given given from Eq.C.2.

$$Rku = \frac{1}{Rq^4} \cdot \frac{1}{l} \int_0^l z^4(x)dx \tag{C.2}$$

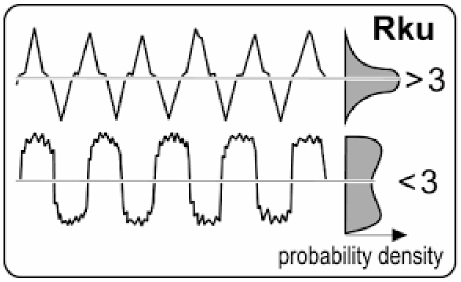

Figure C.2: Definition of Rku metric.

List of Figures

Bibliography

1. Fowles GR. Introduction to Modern Optics. Second edition. Dover Publications (1989)
2. Hecht E. Optics. Fifth edition. Pearson Education (2017)
3. Hecht E. Optics. Fourth edition. Pearson Education (2002)
4. Joanna Schmit and Anna Paluka, Handbook of advanced nondestructive evaluation, chapter 4, white light interferometry, Springer international publishing (2018)
5. Muhammad Rizwan Amirzada, Thesis Phd, Optimization in the Technological Steps for the Fabrication of Large Area Micromirror Arrays, Electrical Engineering and Informatics University of Kassel (2014)
6. Purcell EM, Morin DJ. Electricity and Magnetism. Third edition. Cambridge University Press (2013)
7. Sharma KK. Optics - Principles and Applications. Academic Press, Elsevier (2006)
8. Wolf E. Introduction to the Theory of Coherence and Polarization of Light. Cambridge University Press (2007)
9. Elias N. Glytsis, Spatial Temporal Coherence (2019)
10. Leonard Mandel, Emil Wolf, Optical Coherence and Quantum Optics. Cambridge University Press (1995)
11. Mitsuo Takeda, Joseph Rosen and Duan Zhihui, ”Space-Time Analogy in Synthetic Coherence Functions Applied to Optical Tomography and Profilometry”, Conference paper, Int. Conf. on Laser Applications and Optical Metrology, At Delhi, India (2003)
12. Laura Takkunen, Eero Huovinen, Mika Suvanto, Tapani A Pakkanen, ”Fabrication and quantitative roughness analysis of hierarchical multiscale polymer surface structures”, Micromechanics and Microengineering 24(5):055017, (2014)

13. D.J. Whitehouse. Handbook of surface and nanometrology, 2_{nd} edition (2011)
14. R. K. Leach, Fundamental principle of nanometrology, 1_{st} ed. Elsevier (2010)
15. Suodong Ma, Chenggen Quan, Rihong Zhu, Cho Jui Tay, and Lei Chen, "Surface profile measurement in white-light scanning interferometry using a three-chip color CCD", Applied Optics, OSA (2011)
16. Patrick Sandoz Gilbert Tribillon, "Profilometry by Zero-order Interference Fringe Identification", Modern Optics (1993)
17. Petr Hlubina, Tadeusz Martynkien, and Waclaw Urbańczyk, "Dispersion of group and phase modal birefringence in elliptical-core fiber measured by white-light spectral interferometry", Optics Express (2003)
18. G. Binnig and H. Rohrer, "Scanning tunneling microscopy", Journal of Research and Development,(2000)
19. G. Binnig and C. F. Quate, "Atomic force microscope", Physical Review Letters, (1986)
20. E. Betzig and J. K. Trautman, "Near-Field optics: microscopy, spectroscopy and surface modification beyond the diffraction limit", Science,(1992)
21. Susan Swapp, University of Wyoming, `http://erc.carleton.edu/research_education/geochemsheets/techniques/SEM.html`
22. D. R. Black and G. G. Long, NIST Recommended Practice Guide: X-Ray Topography, Special Publication 960-10 (National Institute of Standards and Technology, 2004).
23. Paris Panagiotopoulos, Master Theis, ¨Φασματοσκοπική Συμβολομετρία με εφαρμογή στη Δυναμική Προφιλομετρία ¨, (2007)
24. Dai Xiaoli, Seta Katuo, "High-accuracy absolute distance measurement by means of wavelength scanning heterodyne interferometry", Measurement Science and Technology,(1998)
25. Zygo Corp., Technical Manual: NewView 5000.
26. Kanik Palodhi, Doctoral Thesis,"Absolute surface topography measurement with polarisation sensitive coherence scanning interferometry ", (2013)
27. Mylan R. Cook, Kent L. Gee, Scott D. Sommerfeldt, and Tracianne B. Neilsen, "Coherence-based phase unwrapping for broadband acoustic signals", (2017).
28. Vangelis Tzardis, diploma thesis "White light interferometry in vision science applications", (2019)